

# Force and torque acting on particles in a transitionally rough open channel flow

Clemens Chan-Braun, Manuel García-Villalba\* and Markus Uhlmann

Institute for Hydromechanics,  
Karlsruhe Institute of Technology,  
76131 Karlsruhe, Germany

July 18, 2018

## Abstract

Direct numerical simulation of open channel flow over a geometrically rough wall has been performed at a bulk Reynolds number of  $Re_b \approx 2900$ . The wall consisted of a layer of spheres in a square arrangement. Two cases have been considered. In the first case the spheres are small (with diameter equivalent to 10.7 wall units) and the limit of the hydraulically smooth flow regime is approached. In the second case the spheres are more than three times larger (49.3 wall units) and the flow is in the transitionally rough flow regime. Special emphasis is given on the characterisation of the force and torque acting on a particle due to the turbulent flow. It is found that in both cases the mean drag, lift and spanwise torque are to a large extent produced at the top region of the particle surface. The intensity of the particle force fluctuations is significantly larger in the large-sphere case, while the trend differs for the fluctuations of the individual components of the torque. A simplified model is used to show that the torque fluctuations might be explained by the spheres acting as a filter with respect to the size of the flow scales which can effectively generate torque fluctuations. Fluctuations of both force and torque are found to exhibit strongly non-Gaussian probability density functions with particularly long tails, an effect which is more pronounced in the small-sphere case. Some implications of the present results for sediment erosion are briefly discussed.

## 1 Introduction

Sediment erosion by turbulent open-channel flow is an important aspect for fluvial engineering applications as it can, for example, cause the collapse of bridges. The mechanisms that lead to sediment erosion however are far from being completely understood due to the complex interactions between the turbulent flow and the sediment particles. Turbulent flow in an open-channel is statistically inhomogeneous in at least one spatial direction, and the Reynolds numbers of interest are typically high, which leads to a wide range of velocity and length scales. In addition, the presence of a range of sediment sizes, shapes and compositions complicates the description. Under certain conditions, the turbulent motions might erode the bed and entrain sediments as a result of the hydrodynamic force and torque acting on the particles. In order to improve the understanding of the mechanisms that lead to sediment erosion it appears necessary to simplify the problem under consideration. Therefore, as a first step we study the statistical properties of hydrodynamic force and torque acting on fixed spherical particles adjacent to the wall-plane in fully-developed, open-channel flow. For this configuration, we have performed direct numerical simulations (DNS).

A wide body of literature exists that focuses on the hydrodynamic force acting on spherical objects placed in a fluid flow. In the low Reynolds number range analytical solutions have been

---

\*Present address: Bioingeniería e Ingeniería Aeroespacial, Universidad Carlos III de Madrid, Leganés 28911, Spain

proposed for various flow configurations, e.g. the case of a particle in a linear shear flow (Saffman, 1965; Auton, 1987), in a non-uniform rotational flow (Auton, Hunt & Prud'homme, 1988), and of a particle in the vicinity of a smooth wall (Krishnan & Leighton, 1995). In order to gain information on the mechanism that leads to lift and drag on a particle in the range from small to moderate Reynolds numbers, similar flow configurations have also been explored by means of experimental studies (King & Leighton, 1997) and by means of direct numerical simulations (Kim *et al.*, 1993; Bagchi & Balachandar, 2002; Zeng *et al.*, 2009; Lee & Balachandar, 2010). In the high Reynolds number limit numerous studies can be found that describe the flow around spheres in unbounded flow (see Yun, Kim & Choi, 2006, for an overview).

The studies mentioned above have focused on situations in which the flow field approaching the sphere is laminar in nature. It is well known, however, that turbulence can have a significant effect on the statistics of the forces acting on a sphere. A review on the effect of turbulence on an isolated sphere can be found in Bagchi & Balachandar (2003). The authors studied the forces on an isolated sphere subject to free-stream isotropic turbulence for small and moderate Reynolds numbers by means of direct numerical simulation. They found that turbulence had only little effect on the mean drag and that the fluctuations of lift and drag scaled linearly with both the mean drag and the turbulence intensity.

In contrast, turbulence appears to have a significant effect in the case of a sphere positioned close to a wall, the lift being particularly affected (Willets & Murray, 1981; Hall, 1988; Zeng *et al.*, 2008). The experimental evidence shows, that similar to the low Reynolds number regime, significant positive values for mean lift (directed away from the wall) are obtained for a sphere touching the wall plane (Willets & Murray, 1981; Hall, 1988; Mollinger & Nieuwstadt, 1996; Muthanna, Nieuwstadt & Hunt, 2005). When the sphere is not touching the wall, the picture is less clear and still a matter of discussion: both positive and negative values of the lift are reported. Willets & Murray (1981) found changes in sign for the value of the mean lift when increasing the wall distance; Hall (1988) measured consistently positive values for various wall distances; Zeng *et al.* (2008) obtained negative values (directed towards the wall) in case the sphere is placed in the buffer layer. Zeng *et al.* (2008) note that the classical formulae based on unbounded shear flow fail to predict their DNS results correctly, stating that further investigations are required to understand the discrepancy.

Hall (1988) showed that the effect of a nearby wall on the lift experienced by a spherical body differs significantly depending on the wall being rough or smooth. In particular, it was found that the lift significantly decreased when the sphere was positioned in between of spanwise oriented, rod-shaped roughness elements. When the sphere was positioned on top of the array of wall-mounted rods, however, the measured lift was comparable to the corresponding smooth-wall values.

The difficulties related to the direct measurement of particle forces as in the studies above have been discussed by Muthanna *et al.* (2005). Another, more indirect approach was taken by Einstein & El-Samni (1949). They approximated the force exerted on hemispheres in an open channel flow by pressure measurements on top and near the bottom of the hemispheres. They reported positive lift on the hemispheres, and were among the first who stated the relevance of the forces on particles in a rough wall to the understanding of sediment erosion. More recent studies following this approach present approximations of lift and drag on cubes, spheres and naturally shaped stones by local pressure measurements (Hofland, Battjes & Booij, 2005; Hofland & Battjes, 2006; Detert, Weitbrecht & Jirka, 2010b). These studies have focused on the higher Reynolds number regime with particle Reynolds numbers of the order of thousands.

The investigations discussed so far have for the most part concentrated on the flow around single spherical objects. Beyond these studies, a large body of literature exists which deals with the characteristics of flow over rough surfaces. Although the precise nature of the fluctuating forces acting on individual roughness elements is often not of interest in the context of studies of roughness effects, findings from that research area are of relevance here. A reference for the earlier work on roughness is Schlichting (1965); a more recent review on the subject, including numerical studies is given by Jiménez (2004). Some aspects of rough-wall flows at high Reynolds number have recently been reviewed by Marusic *et al.* (2010), in particular the question whether

roughness does indeed modify the turbulence structure in the outer flow or simply provides a modified friction velocity.

The research on rough wall turbulence focuses almost exclusively on the effect of the rough wall on the fluid. Some of the key questions of interest are how roughness influences the turbulence structure, what are the consequences for scaling, and how can the effect on the fluid be estimated from the roughness geometry.

Numerical studies of rough wall flows are very demanding in terms of computational cost, much more so than comparable simulations of flow over smooth walls. Therefore, far less direct numerical studies of flow over rough walls have been carried out so far in contrast to flows over smooth wall. Recently a direct numerical study of a boundary layer over surfaces roughened by rectangular spanwise bars and cubes has been carried out by Lee & Sung (2007) and Lee, Sung & Krogstad (2011). Direct numerical simulation of channel flow over a wall similarly roughened by spanwise-oriented square bars has been carried out by Leonardi *et al.* (2003, 2007) among others, while Orlandi & Leonardi (2008) have simulated plane channel flow including different layouts of wall-mounted cubes. Direct numerical simulations of channel flow with wall velocity disturbances (acting as artificial roughness) have been carried out by Orlandi *et al.* (2003) and Flores & Jiménez (2006). More in line with the present setup, Singh, Sandham & Williams (2007) have performed simulations of open channel flow over spheres in hexagonal arrangement, albeit at considerably coarser resolution than the one employed in the present study.

As a first step to understand the mechanism leading to sediment erosion here we present high-fidelity data on the flow over a rough wall with a regular array of fixed spheres. In contrast to most previous studies on roughness, the emphasis of the present work is on the effect of the turbulence on the spherical elements which form the rough wall, including the characteristics of hydrodynamic force and torque.

The article is structured as follows. In §2 the setup of the simulation is described and basic definitions are given. The section also includes a brief discussion of the numerical scheme used. In §3 the results are discussed and compared with previous findings in the literature when possible. The results of the time and spatially averaged flow field statistics are discussed in §3.1, followed by a discussion of the time-averaged three-dimensional flow field statistics in §3.2. The statistics of the particle force and particle torque respectively are presented in §3.3 and §3.4, jointly with their probability density function (pdf) and the local surface distribution of the contribution to the mean values. In the discussion the results are related to some degree to forces and torque on an area element in a smooth wall channel flow. Conclusions and an outlook are given in §4.

## 2 Flow configuration

The flow configuration consists of turbulent open channel flow over a geometrically rough wall. The wall is formed by one layer of fixed spheres which are packed in a square arrangement (see figure 1). The distance between the particle centres is  $D + 2\Delta x$ , where  $D$  is the particle diameter and  $\Delta x$  is the grid spacing. At  $y = 0$  a rigid wall is located below the layer of spheres. As can be seen in figure 1 this rigid wall is roughened by spherical caps that can be defined as the part above  $y = 0$  of spheres located at  $y = D/2 - \sqrt{2}(D/2 + \Delta x)$ , staggered in the streamwise and spanwise direction with respect to the layer of spheres above.

The physical and numerical parameters of the simulations are summarised in table 1. The computational domain dimensions are  $L_x/H \times L_y/H \times L_z/H = 12 \times 1 \times 3$ , in streamwise, wall-normal and spanwise direction, respectively. An equidistant Cartesian grid with  $3072 \times 256 \times 768$  grid points is employed.

One important parameter is the ratio between the domain height,  $H$ , and the spheres diameter,  $D$ . Ideally, a large  $H/D$  is desirable to ensure that the spheres can be considered as roughness and not as obstacles in a channel (Jiménez, 2004). However, from a practical point of view it is difficult to reach large values of  $H/D$  without increasing excessively the computational cost. In this work, two cases are considered: case F10 with  $H/D = 18.3$  and a total of 9216 particles, and case F50 with  $H/D = 5.6$  and a total of 1024 particles above the bottom wall.

Case	$U_{bh}/u_\tau$	$Re_b$	$Re_\tau$	$D^+$	$D/\Delta x$	$\Delta x^+$	$N_p$	$\mathcal{T}_c U_{bH}/H$
F10	15.2	2870	188	10.7	14	0.77	9216	120
F50	12.2	2880	235	49.3	46	1.07	1024	120

Table 1: Setup parameters of simulations;  $U_{bH}$  is the bulk velocity based on the domain height  $H$ ,  $U_{bh}$  is the bulk velocity based on the effective flow depth  $h$  defined as  $h = H - 0.8D$ ,  $u_\tau$  is the friction velocity,  $Re_b = U_{bH}H/\nu$  is the bulk Reynolds number,  $Re_\tau = u_\tau h/\nu$  is the friction Reynolds number,  $D^+ = Du_\tau/\nu$  is the particle diameter in viscous units,  $D/\Delta x$  is the resolution of a particle,  $\Delta x^+$  is the grid spacing in viscous units,  $N_p$  is the total number of particles in a layer,  $\mathcal{T}_c$  is the time over which statistics were collected.

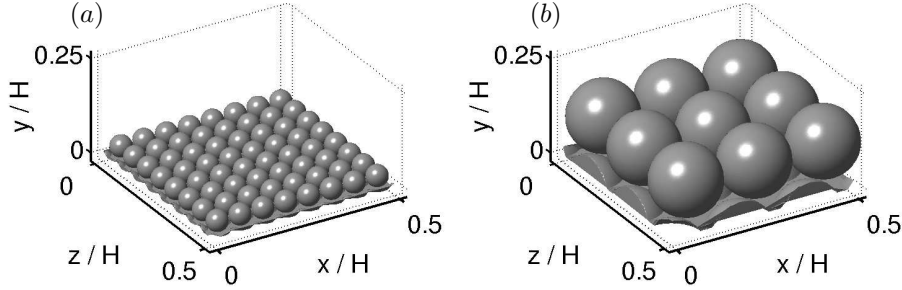


Figure 1: Close-up of a section of the computational domain with the geometry of the bottom wall consisting of a layer of fixed spheres arranged on a square lattice; (a) case F10; (b) case F50.

Periodic boundary conditions are applied in streamwise and spanwise directions. At the upper boundary a free-slip condition is employed. At the bottom boundary a no-slip condition is applied. The spheres are resolved using the immersed boundary method which is described in §2.1.

In order to scale the results, two quantities need to be specified: the friction velocity  $u_\tau$  and the location of the virtual wall,  $y_0$ , since for a geometrically rough wall the position of the wall cannot be unambiguously defined (cf. Townsend, 1971; Raupach *et al.*, 1991). As discussed in detail in appendix §A, we choose to define the position of the virtual wall as  $y_0 = 0.8D$  throughout this study. The value of  $u_\tau$  is defined by extrapolating the total shear stress  $\tau_{tot} = \rho\nu\partial\langle u \rangle/\partial y - \rho\langle u'v' \rangle$  from above the roughness layer (where it varies linearly) down to the location of the virtual wall  $y_0$ . The effective flow depth,  $h$ , can be defined as the distance from the virtual wall to the top boundary,  $h = H - y_0$ . The bulk velocity based on the domain height,  $H$ , is defined as  $U_{bH} = 1/H \int_0^H \langle u \rangle dy$ ; the bulk velocity based on the effective flow depth is defined as  $U_{bh} = 1/h \int_{y_0}^H \langle u \rangle dy \approx U_{bH}H/h$ . Angular brackets are used for the notation of the averaging operator jointly with sub-indexes  $t, x_i, p$  in order to specify averaging in time, along the direction  $x_i$  or over the periodically repeating cells of the geometry, respectively. Angular brackets without additional indices refer to quantities which are averaged over time as well as spatially over wall-parallel planes, i.e. along the  $x$  and  $z$  directions. The bulk Reynolds number,  $Re_b = U_{bH}H/\nu$ , was kept constant at a value of 2870 and 2880 in cases F10 and F50, respectively. This corresponds to a friction Reynolds number,  $Re_\tau = u_\tau h/\nu \simeq 180$  in case of a smooth wall. In the present simulation the value for  $Re_\tau$  increases to 188 in case F10 and to 235 in case F50.

The grid resolution of the simulation was in both cases approximately equal to the viscous length  $\delta_\nu = \nu/u_\tau$  in all spatial directions. The resolution can therefore be qualified as exceptionally fine away from the wall and as reasonably fine in the vicinity of the wall. In the following, normalisation with wall units will be denoted by a superscript  $+$ .

The initial turbulent flow field of each simulation was taken from a similar simulation on a coarser grid. Subsequently, the simulation was run until the flow reached a statistically-stationary state. The simulation was then continued for  $120 H/U_{bH}$  during which flow field statistics as

well as particle data such as forces and torques were collected. Entire flow fields jointly with the particle data were stored at intervals of about  $H/U_{bH}$ . Based on these data a statistical analysis has been carried out. If not explicitly stated otherwise, the statistics shown in the following stem from the data collected during the runtime of the simulation and are averaged over the entire domain including the region within the particles. Details on the different averaging procedures used and how they compare are provided in §B and §C.

## 2.1 Numerical scheme

In order to discretise the complex shape of the wall (cf. figure 1), the present simulations were carried out with the aid of a variant of the immersed boundary technique (Peskin, 1972, 2002) proposed by Uhlmann (2005a). This method employs a direct forcing approach, where a localised volume force term is added to the momentum equations. The additional forcing term is explicitly computed at each time step as a function of the no-slip condition at the fixed particle surface, without resorting to a feed-back procedure. The necessary interpolation of variable values from Eulerian grid positions to particle-related Lagrangian positions (and the inverse operation of spreading the computed force terms back to the Eulerian grid) are performed by means of the regularised delta function given by Roma, Peskin & Berger (1999).

A Cartesian grid with uniform isotropic mesh width  $\Delta x = \Delta y = \Delta z$  is employed which ensures that the regularised delta function verifies important identities (such as the conservation of the total force and torque during interpolation and spreading). For reasons of efficiency, forcing is only applied to the surface of the spheres, leaving the flow field inside the particles to develop freely.

The immersed boundary technique is implemented in a standard fractional-step method for the incompressible Navier–Stokes equations. The temporal discretisation is semi-implicit, based on the Crank–Nicholson scheme for the viscous terms and a low-storage three-step Runge–Kutta procedure for the non-linear part (Verzicco & Orlandi, 1996). The spatial operators are evaluated by central finite-differences on a staggered grid. The temporal and spatial accuracy of this scheme are of second order.

An important benefit for the present simulation is that the hydrodynamic forces acting upon a particle are readily obtained by summing the additional volume forcing term over all discrete forcing points. The analogue procedure is applied for the computation of the hydrodynamic torque.

The present numerical method has been submitted to exhaustive validation tests (Uhlmann, 2003, 2005a,b, 2006a), as well as grid convergence studies (Uhlmann, 2006b). In addition, the computational code has been applied to the case of vertical plane channel flow with many moving particles (Uhlmann, 2008). In particular, this reference also includes a validation against the benchmark case of Kim *et al.* (1987). Recently, the present immersed boundary method has been successfully implemented and employed in different numerical codes by other researchers (e.g. Lucci, Ferrante & Elghobashi, 2010; Lee & Balachandar, 2010).

## 3 Results and discussion

### 3.1 Flow field statistics

Figure 2 shows the profiles of the time and plane averaged streamwise velocity component,  $\langle u \rangle$ , as a function of the vertical coordinate. The results of case F10 and case F50 are compared with the reference case S180 of a smooth-wall open-channel flow at  $Re_b = 2880$  and  $Re_\tau = 183$ , which has been recomputed for the present study. The profiles show the expected effect of roughness that is described in various textbooks (Schlichting, 1965; Pope, 2000). As the particle diameter  $D$  increases, while keeping the value of the bulk Reynolds number  $Re_b$  constant, the friction velocity increases; the streamwise velocity profile normalised by outer scales flattens (figure 2a), and the streamwise velocity profile normalised by viscous scales increasingly shifts towards lower values of  $\langle u \rangle^+$  (figure 2b). Figure 2 shows that a logarithmic layer exists, if at all, only over a small range

due to the low Reynolds number considered. The logarithmic law for the flow over a rough wall can be written as in the case of a smooth wall with an additional offset  $\Delta U^+$  that accounts for the roughness effect

$$\langle u \rangle^+ = \frac{1}{\kappa} \ln \left( \frac{y - y_0}{\delta_\nu} \right) + A - \Delta U^+, \quad (1)$$

where  $\kappa$  and  $A$  are constants obtained empirically to be  $\kappa \approx 0.4$  and  $A \approx 5.1$  (according to experimental findings summarized e.g. in Jiménez, 2004). From the profiles in figure 2 it appears that in case F10 the roughness effect is weak, while in case F50 a stronger roughness effect can be seen.

It is customary to quantify the roughness effect by using the equivalent sand grain roughness  $k_s$  (Schlichting, 1936). It can be obtained by a fit to the mean velocity profile in the logarithmic layer using the following equation

$$\langle u \rangle^+ = C \log_{10} \left( \frac{y - y_0}{k_s} \right) + B, \quad (2)$$

where  $B \approx 8.48$  and  $C = 1/\kappa \ln(10) \approx 5.75$  are empirically obtained values (cf. Shockling, Allen & Smits, 2006). At high enough Reynolds numbers  $k_s$  becomes constant, i.e.  $\lim_{Re \rightarrow \infty} k_s = k_{s\infty}$ , defining the so-called fully rough flow regime. The specific value of  $k_{s\infty}$  is a property of the surface that depends on the characteristics of the roughness, such as shape, arrangement or roughness area ratio. Flow over roughness can be classified as hydraulically smooth, transitionally rough or fully rough according to a small, moderate or high value of  $k_{s\infty}^+$ . Nikuradse (1933) gave values of  $5 < k_{s\infty}^+ < 70$  to define the transitionally rough flow regime. However, these values should be taken with care as the transition might be influenced by the specific characteristics of the roughness (cf. discussion in Bradshaw, 2000; Jiménez, 2004; Shockling *et al.*, 2006, among others). In particular, it has been speculated that a uniformly sized, structured arrangement of roughness elements as in the present case might lead to a sharp transition from hydraulically smooth to the fully rough regime (Colebrook, 1939; Jiménez, 2004). Figure 3 shows the transition from the hydraulically smooth flow regime to the fully rough flow regime obtained in different experiments. It shows the offset  $\Delta U^+$  as a function of  $k_{s\infty}^+$ . At low values of  $k_{s\infty}^+$  the effect of roughness should be negligible and correspondingly  $\Delta U^+$  approaches zero. In the fully rough flow regime the roughness effect should purely depend on  $k_{s\infty}^+$ . Comparing equations (1) and (2) a formula for  $\Delta U^+$  can be derived for the fully rough regime,

$$\Delta U^+ = C \log_{10} (k_{s\infty}^+) - B + A, \quad (3)$$

with the constants  $A, B$  and  $C$  as above. The relation (3) above is shown in figure 3 jointly with results from experiments.

For the present simulations the values of  $\Delta U^+$  can be obtained by the vertical shift of the mean velocity profiles in the log-region of figure 2(b). They are 1.03 and 4.85 for cases F10 and F50, respectively. However, the value of  $k_{s\infty}/D$  for the present arrangement of spheres is unknown. Schlichting (1936), Ligrani & Moffat (1986) and Pimenta, Moffat & Kays (1975) found a value of  $k_{s\infty}/D \sim 0.63$  for flow over spheres in hexagonal packing, while somewhat larger values were obtained by Singh *et al.* (2007) ( $k_{s\infty}/D = 0.77$ ) and Detert *et al.* (2010a) ( $k_s/D = 0.81$ ). For flow over spheres in random packing the values generally obtained vary in the range of  $k_{s\infty}/D = 0.55$  to  $0.85$  (cf. Muñoz Goma & Gelhar, 1968; Grass *et al.*, 1991). Few studies exist that use values of  $k_{s\infty}/D = 1$  for structured (Einstein & El-Samni, 1949) or random arrangements (Nakagawa & Nezu, 1977). Figure 3 shows the pair of values ( $k_{s\infty}^+, \Delta U^+$ ) for cases F10 and F50 when approximating  $k_{s\infty}/D$  by the value found for a hexagonal packing, i.e.  $k_{s\infty}/D = 0.63$ . The error-bars indicate the range of  $k_{s\infty}/D = 0.55$  to  $1$  as found in the literature. It can be seen that case F10 approaches the hydraulically smooth flow regime while case F50 is in the transitionally rough flow regime.

A similar conclusion can be reached by analysing the profiles of the root-mean-square of the velocity fluctuations normalised with  $u_\tau$  that are shown in figure 4(a). In case F10, the profiles of the

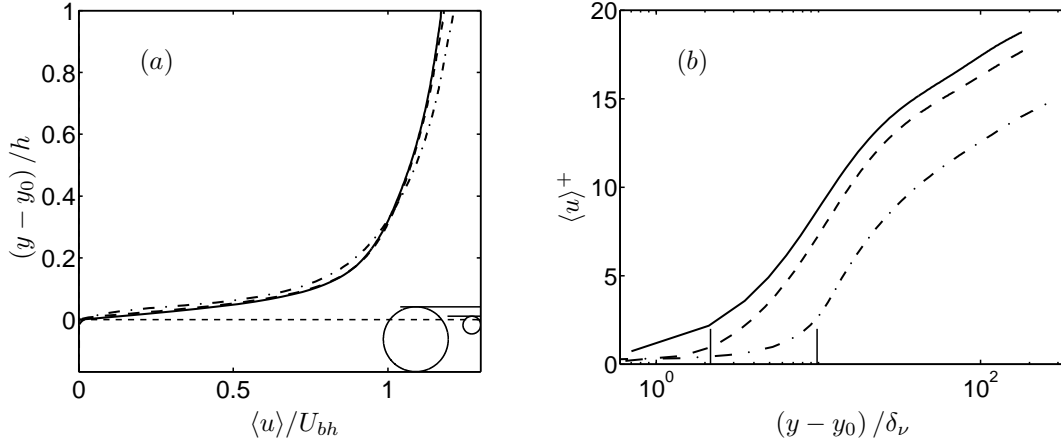


Figure 2: Time and spatially averaged streamwise velocity component  $\langle u \rangle$  of case F10 (dashed line) and case F50 (dashed dotted line) in comparison with smooth wall open channel flow (continuous line); (a): normalised with  $U_{bh}$  as a function of  $(y - y_0)/h$ ; (b): in semi-logarithmic scale normalised by  $\delta_\nu$  and  $u_\tau$ ; the position of the particles top are marked with horizontal (a) and vertical (b) solid lines.

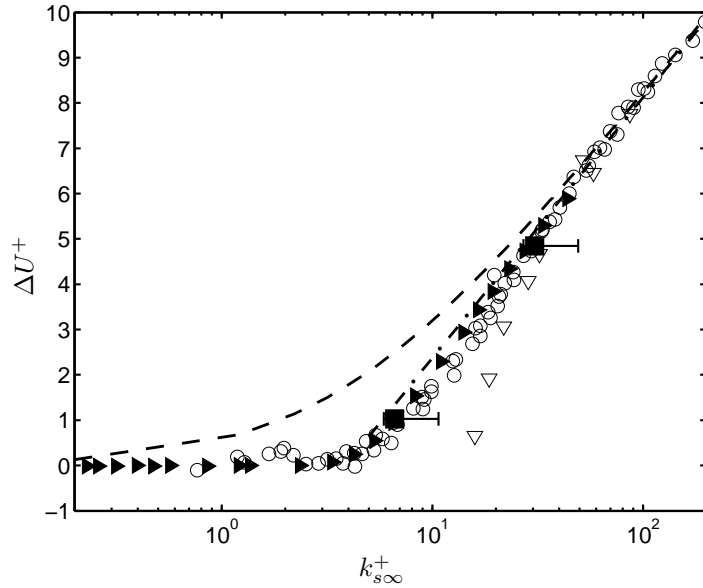


Figure 3: Roughness function for several transitionally rough surfaces as a function of the Reynolds number based on  $k_{s\infty}^+$  adapted from Jiménez (2004). ○, Nikuradse (1933), uniform sand, pipe flow; ▽, Ligrani & Moffat (1986), uniform densely-packed spheres, boundary layer; ►, Shockling *et al.* (2006), honed aluminium, pipe flow; ■, present simulation with  $k_{s\infty}/D = 0.63$ , error-bars show the range of  $k_{s\infty}/D = 0.55$  to 1; dashed line,  $\Delta U^+ = 5.75 \log(1 + 0.26 k_{s\infty}^+)$  proposed by Colebrook (1939); dashed dotted line, relation (3) with  $A = 5.1$ ,  $B = 8.48$  and  $C = 5.75$ .

three velocity components almost collapse with the smooth-wall results, indicating that, indeed, the flow over the relatively small roughness elements in this case can be considered as nearly hydraulically smooth. In case F50, some differences with respect to the smooth wall case are evident. The near-wall peak in the streamwise fluctuation profile decreases but it is still visible. This indicates that the flow is in the transitionally rough flow regime since experiments in the fully rough flow regime present no clear peak (see for example figure 5 of Jiménez, 2004). The wall-normal and spanwise fluctuations present slightly higher values near the wall than the corresponding ones in the smooth-wall case. Therefore, the anisotropy of the fluctuations near the wall is smaller than in the smooth-wall case. This tendency of roughness to make the fluctuations more isotropic is a phenomenon which has been often reported in the literature (e.g. Poggi, Porporato & Ridolfi, 2003; Orlandi & Leonardi, 2008). Also in case F50, above  $(y - y_0)/h \sim 0.4$  all three components agree well with the values of the smooth-wall case.

Orlandi & Leonardi (2008) discuss the velocity shift  $\Delta U^+$  as a function of  $v_{rms}$  at the roughness crest. The present simulations result in pairs  $(v_{rms}, \Delta U^+)$  of (0.10, 1.03) (0.46, 4.85) for case F10 and F50 respectively which agree well within the scatter of the reported data (graph not shown).

Figure 4(b) shows the profiles of the Reynolds stress,  $\langle u'v' \rangle$ , normalised by  $u_\tau^2$ . The Reynolds stress profile  $\langle u'v' \rangle$  of case F10 nearly collapses with the profile of the smooth-wall case. In case F50 a slight increase and a small shift towards the wall of the near-wall peak can be seen which could be an effect of the higher value of  $Re_\tau$  in this case.

In order to study the near wall behaviour of the velocity fluctuations, a close-up of the profiles shown in figure 4(a), is plotted as a function of  $(y - y_0)/D$  in figure 5. Additionally, the profiles of the root-mean-square of the pressure fluctuations,  $p_{rms}/(\rho u_\tau^2)$ , are included. Note that in contrast to figure 4 the profiles shown in figure 5 are obtained from snapshots of the flow field and obtained by averaging over cells outside of the particles as described in detail in §B and §C. The amplitudes of the fluctuations of the three velocity components present similar values below the virtual wall,  $(y - y_0)/D < 0$ . These are much smaller than the values above the virtual wall, and they are somewhat larger in case F50 ( $u_{rms}^i \sim 0.1u_\tau$ ) compared to F10 ( $u_{rms}^i < 0.05u_\tau$ ). On the contrary, the pressure fluctuations within the roughness layer for both cases present values which are similar to the values above the roughness layer.

Recall that also in the case of a smooth wall the pressure fluctuations are non-zero at the wall (Kim, Moin & Moser, 1987; Kim, 1989). Near the top of the roughness elements, i.e. around  $(y - y_0)/D = 0.2$ , the profiles of  $p_{rms}$  exhibit a peak which is barely visible in case F10 and more pronounced in case F50. In case F50 the value of the peak is higher by a factor of two compared to case F10. Note that the peak is, to some extent, a consequence of the three-dimensionality of the time-averaged flow field around the particle; this point is further elaborated in §3.2. The pressure fluctuation profiles of case F10 and F50 (when plotted as a function of  $(y - y_0)/h$ ) approach each other with increasing wall distance (not shown). They converge to the profile obtained in the case of a smooth wall in the outer part of the flow.

### 3.2 Three-dimensional time-averaged flow field distribution

Since the geometry of the roughness is three-dimensional the time-averaged flow field in the near wall region also varies in all three directions. In the following some characteristics of the time-averaged flow field obtained from 90 snapshots are discussed. In addition to the averaging in time the fields were averaged over periodically repeating boxes centred on the particles (henceforth indicated by the symbol  $\langle \cdot \rangle_{tp}$ ). For simplicity this will be simply referred to as time averaging below.

Figure 6 shows the distribution of the three-dimensional time-averaged streamwise velocity,  $\langle u \rangle_{tp}$ , for both cases. Two different  $(x, y)$ -planes are shown. The first one contains the centre of the particles of one streamwise row (figure 6a and figure 6c). The second one is located in between two streamwise rows of particles (figure 6b and figure 6d). As can be expected the flow field is very different from a single sphere in an unbounded turbulent flow or in a channel close to a wall (Bagchi & Balachandar, 2004; Zeng *et al.*, 2008).



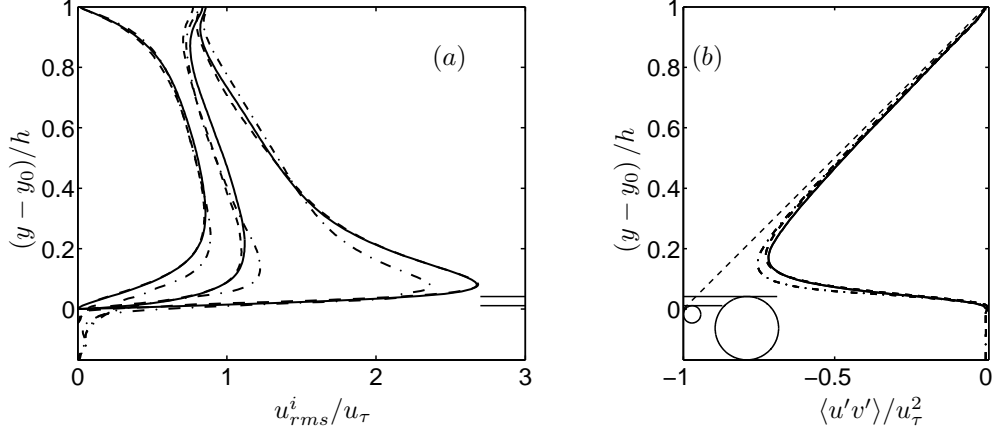


Figure 4: (a) Root-mean-square of velocity fluctuations of case F10 and case F50 normalised by  $u_\tau$  in comparison with results of smooth wall as a function of wall distance; curves from left to right wall-normal ( $v_{rms}/u_\tau$ ), spanwise ( $w_{rms}/u_\tau$ ) and streamwise ( $u_{rms}/u_\tau$ ); (b): distribution of Reynolds shear stress  $\langle u'v' \rangle$  as a function of wall distance. Legend as in figure 2. The position of the particle tops are marked with horizontal solid lines. In (b) the straight dashed line is included to guide the eye.

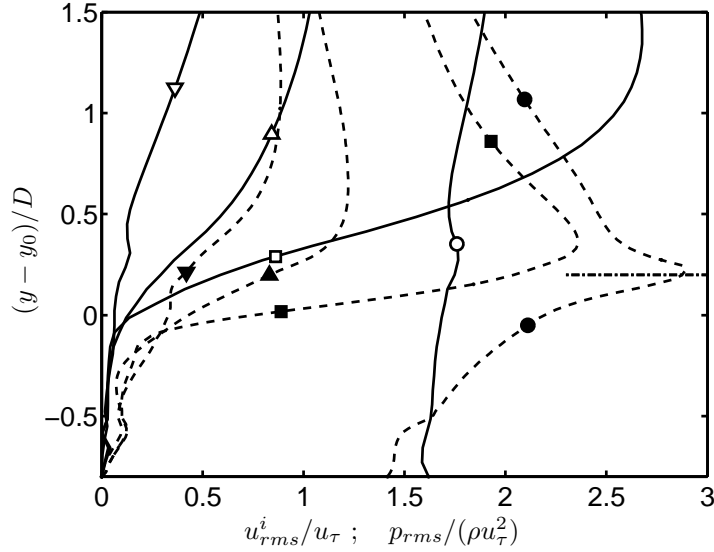


Figure 5: Root-mean-square of velocity and pressure fluctuations of case F10 and case F50, normalised by  $u_\tau$  and  $\rho u_\tau^2$  respectively, as a function of  $(y-y_0)/D$ ; averaging has been carried out over fluid cells only, for details see §B;  $\square$  :  $u_{rms}/u_\tau$ ,  $\nabla$  :  $v_{rms}/u_\tau$ ,  $\triangle$  :  $w_{rms}/u_\tau$ , and  $\circ$  :  $p_{rms}/\rho u_\tau^2$ ; solid lines and empty symbols: case F10, dashed lines and full symbols: case F50; horizontal line: position of particle tops in both cases.

The sheltering effect of the neighbouring particles causes the flow velocity to decrease rapidly close to the roughness tops and leads to marginal flow velocities within the roughness layer. The highest velocity gradients are produced in the vicinity of the roughness tops. Similar observations were made in the experiments of Pokrajac & Manes (2009) who studied a comparable particle arrangement at bulk Reynolds numbers of order  $10^4$  and a ratio of  $h/D \approx 3.5$ . Also similar to their results is the formation of a recirculation between two spanwise rows of spheres that extends over the entire spanwise direction. The shape of the recirculation is similar in both of our present cases, however the strength differs. In case F50 the backflow velocities reach values as low as  $\langle u \rangle_{tp} \approx -0.4u_\tau$  in figure 6(c) and  $\langle u \rangle_{tp} \approx -0.2u_\tau$  in figure 6(d). In case F10 the magnitude of the backflow velocity is below  $0.05u_\tau$ . The recirculation can also be observed in figure 7 that shows streamlines of the mean flow projected into the same planes shown in figure 6, i.e. by computing the streamlines using only  $\langle u \rangle_{tp}$  and  $\langle v \rangle_{tp}$ , together with contours of the time-averaged pressure field. The pressure distributions in both simulations are similar. However, in case F10 the magnitude of the pressure,  $\langle p \rangle_{tp}/(\rho u_\tau^2)$ , is a factor of two smaller compared to case F50. Please note that the three-dimensional time-averaged flow is not fully converged and at the location of the planes shown in figure 7 there is a weak net flow in the spanwise direction with a maximum amplitude of  $\langle w \rangle_{tp} \approx 4 \cdot 10^{-4}U_{bh}$  ( $6 \cdot 10^{-4}U_{bh}$ ) in case F10 (F50). This net flow is within the range of the statistical uncertainty.

A question of interest is how far the three-dimensionality of the bottom wall directly influences the flow. Figure 7 already shows that one particle diameter above the roughness tops the time-averaged pressure field is still visibly affected. In order to quantify the effect of three-dimensionality, the difference between the time-average of a field  $\langle \phi \rangle_{tp}$  (where  $\phi$  can stand for either pressure or one of the velocity components) and its time and plane-averaged value,  $\langle \phi \rangle$ , can be defined, viz.

$$\phi'' = \langle \phi \rangle_{tp} - \langle \phi \rangle. \quad (4)$$

Note that the quantity defined by (4) is sometimes called spatial disturbance in the context of the double-averaging methodology (Nikora *et al.*, 2001). From equation (4) the corresponding standard deviation  $\phi''_{rms} = \sqrt{\langle \phi'' \phi'' \rangle}$  can be computed. In both cases, F10 and F50, the standard deviation of pressure  $p''_{rms}$  drops by several orders of magnitude in between  $y = D$  and  $y = 2D$ , as shown in figure 8. The same is true for the velocity field (not shown). Therefore, the time-averaged flow statistics appear to be essentially one dimensional beyond wall distances of  $2D$ . This is somewhat smaller than the values reported in previous investigations of flow over rough walls (cf. Jiménez, 2004) which might be related to the low values of  $D^+$  and  $Re_\tau$  considered.

### 3.3 Statistics of particle forces

The hydrodynamic force,  $\mathbf{F}$ , acting on a particle is defined as

$$\mathbf{F} = \int_{\Gamma} \boldsymbol{\tau} \cdot \mathbf{n} \, d\Gamma - \int_{\Gamma} p^{tot} \mathbf{n} \, d\Gamma, \quad (5)$$

where  $\Gamma$  is the sphere's surface,  $\mathbf{n}$ , is the surface normal vector,  $\boldsymbol{\tau} = \rho\nu(\partial_j u_i + \partial_i u_j)$  is the viscous stress tensor and  $p^{tot}$  is the pressure. The latter can be split into two parts  $p^{tot} = p + p_l$ , where  $p_l$  represents the linear variation in streamwise direction which results from the imposed pressure-gradient that drives the flow, and  $p$  corresponds to the three-dimensional instantaneous fluctuation. The first term on the right hand side of equation (5) is the force due to viscous stresses, the second term is the force due to pressure. A sketch that illustrates the definition of the force on a particle can be seen in figure 9(a).

In order to scale the hydrodynamic forces, reference quantities need to be defined. For the present case of particles within a roughness layer the subject is a matter of discussion and several definitions have been proposed in the literature (see Hofland *et al.*, 2005). Here, the reference force is defined as  $F_R = \rho u_\tau^2 A_R$  with the reference area  $A_R = L_x L_z / N_p$ .

Table 2 summarises the particle force statistics of the two cases, where  $C_F^{x_i}$  is the mean force on a particle in  $x_i$ -direction normalised by  $F_R$ . As can be seen, the mean values of the forces acting in

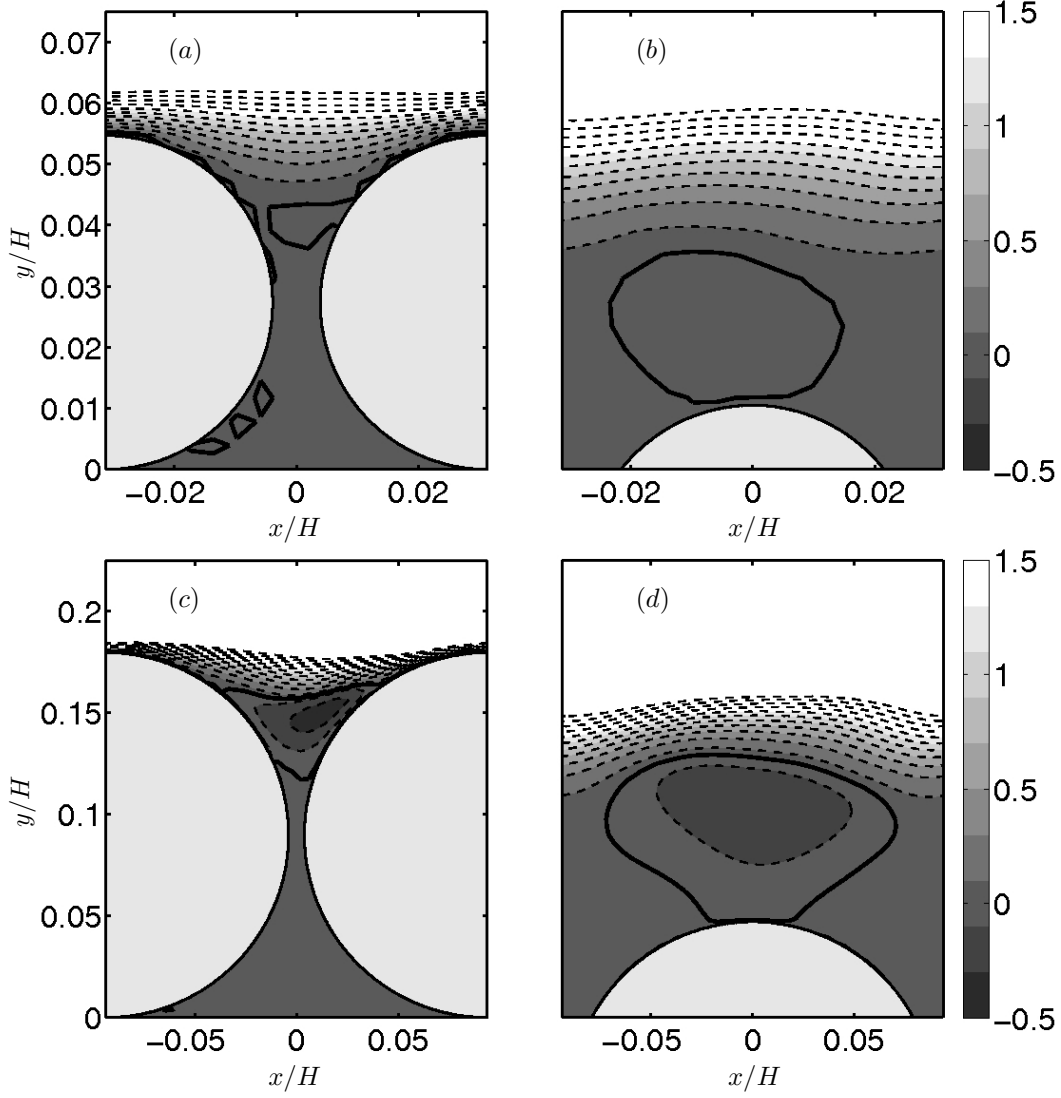


Figure 6: Distribution of the time-averaged streamwise velocity in a periodic cell,  $\langle u \rangle_{tp}$ , normalised by  $u_\tau$  in  $x$ - $y$  planes; (a, c) show a plane through particle centres, (b, d) show a plane centred between spheres. Dashed lines: iso-contours of  $\langle u \rangle_{tp}$  at values of -0.5 to 2.1 in steps of 0.2; black solid line: streamwise velocity contour at  $-10^{-3}$ . Panels (a) and (b) show case F10, (c) and (d) show case F50. The direction of the bulk velocity is from left to right in all panels.

Case	$C_F^x$	$C_F^y$	$C_F^z$	$\alpha_F$	$\sigma_F^x/F_R$	$\sigma_F^y/F_R$	$\sigma_F^z/F_R$	$S_F^x$	$S_F^y$	$S_F^z$	$K_F^x$	$K_F^y$	$K_F^z$
F10	1.04	0.19	0.00	$11^\circ$	0.57	0.20	0.66	0.18	1.80	0.01	10.13	19.08	9.92
F50	1.15	0.37	0.00	$18^\circ$	1.32	0.66	1.26	0.06	0.26	0.01	4.98	5.68	4.29

Table 2: Statistics of particle forces in case F10 and case F50, where  $C_F^{x_i} = \langle F^{x_i}/F_R \rangle$  is the normalised mean force component in the  $x_i$ -direction,  $\alpha = \arctan(C_F^y/C_F^x)$  is the angle of the resulting force with respect to the  $x$ -axis,  $\sigma_F^{x_i}$  is the normalised standard deviation of the force in  $x_i$ ,  $S_F^{x_i}$  and  $K_F^{x_i}$  are the skewness and kurtosis of the respective force component.

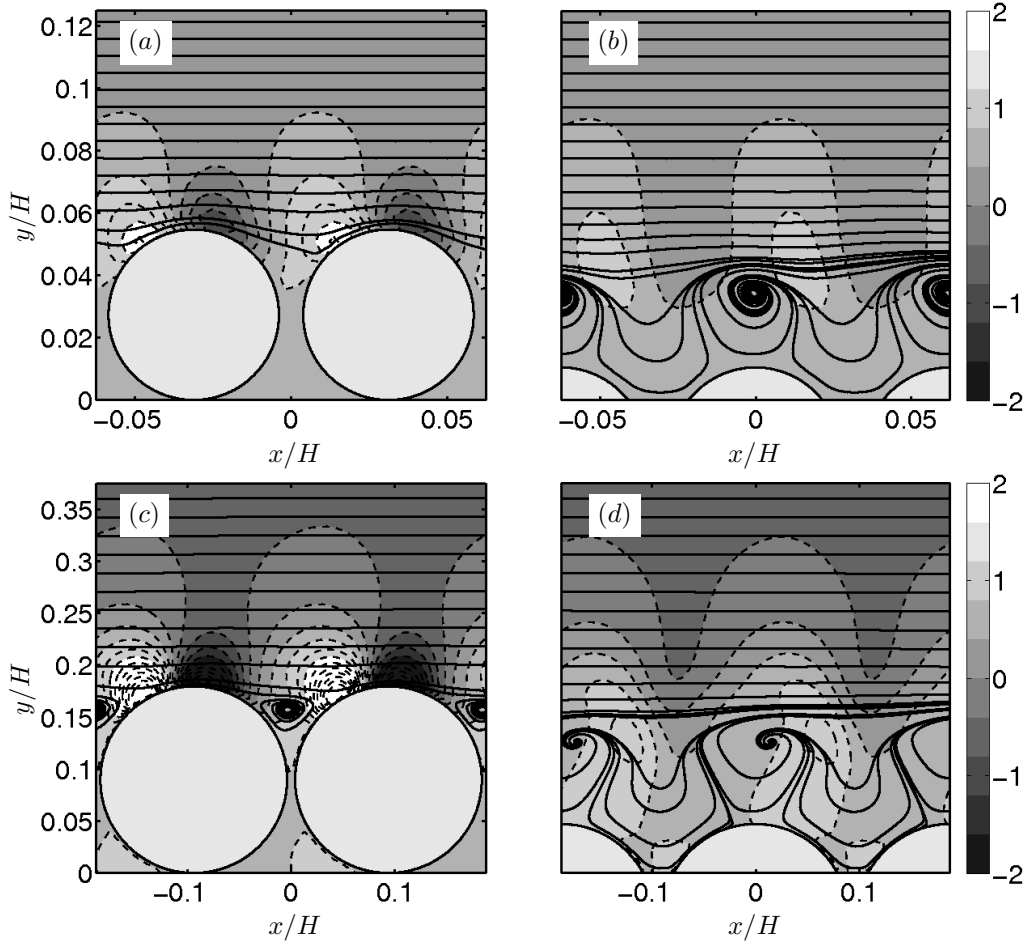


Figure 7: As figure 6 but showing the time-averaged pressure field and corresponding streamlines; dashed lines: iso-contour lines of pressure,  $\langle p \rangle_{tp} / (\rho u_\tau^2)$ , from values of -4 to 4 in steps of 0.4; continuous lines: streamlines in the plane computed from  $\langle u \rangle_{tp}$  and  $\langle v \rangle_{tp}$ . The direction of the bulk velocity is from left to right in all panels.

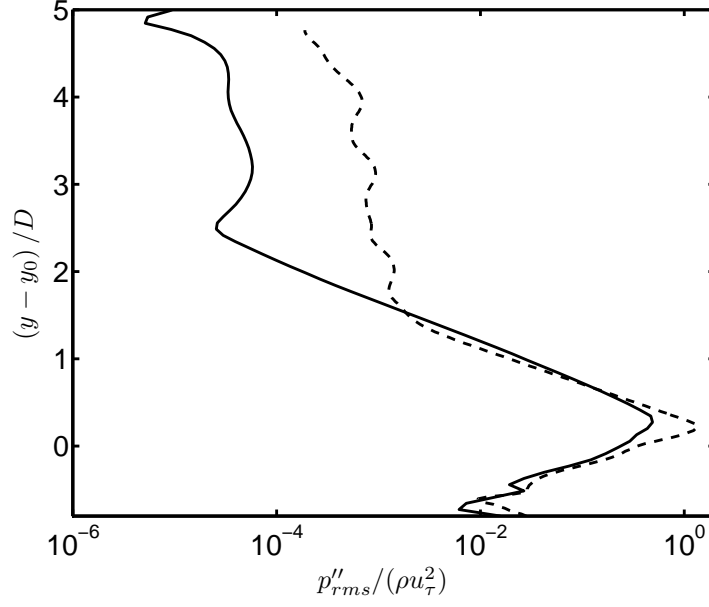


Figure 8: Three-dimensionality of the time-averaged flow field as a function of wall distance quantified via  $p''_{rms}$  (defined in 4). Solid lines: case F10 ; dashed lines: case F50.

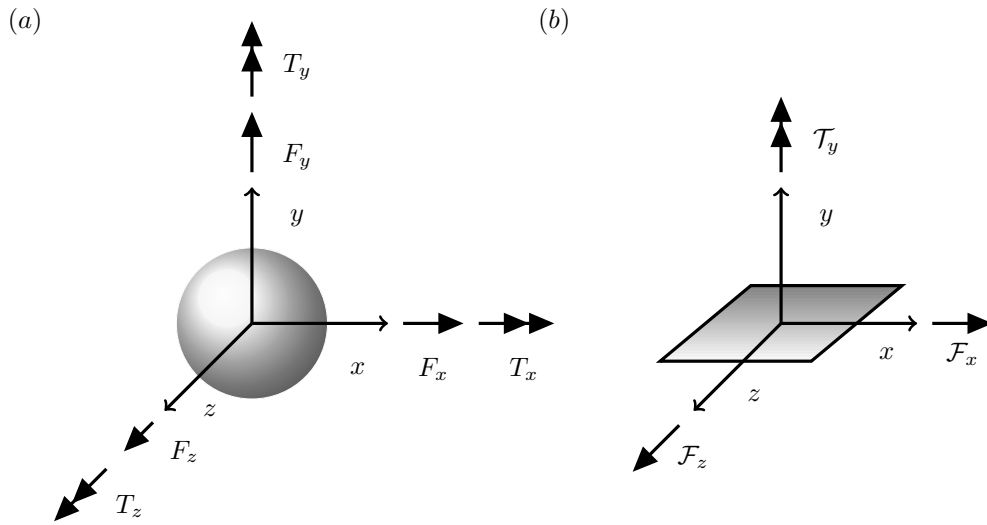


Figure 9: Sketch illustrating the definition of force ( $\rightarrow$ ) and torque ( $\rightarrow\rightarrow$ ) on a particle (a) and a square surface element in a smooth-wall channel (b)

the streamwise direction (henceforth also called “drag”) and the wall-normal direction (“lift”) are positive. Since the mean forces are directly related to the mean flow through the time-averaged version of equation (5), it is possible to shed some light onto the mechanisms that lead to drag and lift by analysing figures 6 and 7. A more detailed picture can be obtained from figure 10 and figure 11 which show the distribution on the sphere’s surface of the stress leading to drag,  $\tau_D$ , and lift,  $\tau_L$ , viz.

$$\tau_D = (\langle \boldsymbol{\tau} \rangle_t \cdot \mathbf{n} - \langle p^{tot} \rangle_t \mathbf{n}) \cdot \mathbf{e}_1, \quad (6)$$

$$\tau_L = (\langle \boldsymbol{\tau} \rangle_t \cdot \mathbf{n} - \langle p^{tot} \rangle_t \mathbf{n}) \cdot \mathbf{e}_2, \quad (7)$$

where  $\mathbf{e}_i$  is the unit vector in the  $x_i$ -direction. The stresses in figures 10 and 11 are normalised by  $F_R/A_{sph}$ , where  $A_{sph} = \pi D^2$  is the surface area of the sphere; by virtue of this normalisation the total integral of the quantities shown in the figures yields the force coefficients  $C_F^{x_i}$  given in table 2. Please note that the results of case F50 appear less smooth due to the smaller number of particles, and therefore a smaller number of samples.

Figure 10 shows that the local stress contributing to drag is similarly distributed over the particle surface in both of our present flow cases F10 and F50. One can observe a region of strong positive values with the largest magnitude centred around a position slightly upstream of the particle tops. From figure 10(a, c) we can see that this region of high positive local contributions to drag is slightly elongated in the spanwise direction. It results from the wall-normal gradients of the average streamwise velocity component which are particularly important in the upper part of the sphere as well as from the high pressure values found near the upstream side of each sphere (cf. figures 6 and 7). On the downstream side of the particles, still in the upper hemisphere, a smaller region with weak negative contributions to drag is found, as a result of the recirculation region. In most of the lower (near-wall) half of the spheres, the contour lines of the local drag contribution are roughly oriented in the wall-normal direction, changing sign slightly downstream of the cross-stream plane passing through the particle centre. In this context it should be noted, that the driving pressure gradient  $dp_l/dx < 0$  makes a weak but non-negligible contribution to the drag which can be quantified as approximately 2% (9%) of  $C_F^x$  in case F10 (F50). Therefore, non-negligible values of local contributions to drag are expected even in relatively quiescent regions, as is the case inside the roughness layer.

The qualitative and quantitative similarity of the distribution of  $\tau_D$  in both cases F10 and F50 results in similar values for the drag coefficient in both cases (cf. table 2). In particular, the overall drag coefficient  $C_F^x$  in case F10 is close to unity, increasing to 1.15 in case F50. These values are a result of the weak contribution of the drag on the rigid wall below the layer of spheres to the total drag on the wall and the choice of the reference force. The drag coefficient as defined in the present study can be approximated as

$$C_F^x \approx \frac{V_f^{(tot)} + V_{sph}}{hA_R}, \quad (8)$$

where  $V_f^{(tot)}$  is the total volume occupied by fluid in a periodic cell around a particle,  $V_{sph}$  is the volume occupied by a particle. The approximation (8) neglects the streamwise component of the shear force acting on the bottom wall in addition to the drag due to the periodic part of the pressure acting on the spherical caps. Evaluating this geometrical relation (8) yields 1.04 (1.15) for case F10 (F50).

Positive values for the lift coefficient, as observed in the present simulations (cf. table 2), can be explained by two mechanisms. The approaching flow accelerates in the frontal part until the top of the sphere and from then on it decelerates. This fact is reflected in the curvature of the streamlines (figures 6a, c), yielding a pressure distribution which exhibits lower values of pressure near the particles tops (figures 7a, c), and therefore a positive lift. In addition to pressure, shear might lead to a positive lift. As can be seen in figure 6, the flow field above the spheres is asymmetric (with respect to a cross-sectional plane through the particle centres) as a result of the recirculation behind the particles. Therefore, the friction on the upstream side of the particle

(in the upper hemisphere) is expected to be higher compared to the corresponding friction on the downstream side, contributing positively to the lift on the particle. The pressure differences as well as the asymmetry of the flow seem to be more pronounced in case F50 than in case F10 and might explain the observed increase in the lift coefficient.

Figure 11 shows the distribution on the sphere’s surface of the stress leading to lift,  $\tau_L$ . The shape of the contours is again similar in both cases, however, the magnitude of the stress  $\tau_L$  seems to be significantly larger in case F50, leading after integration to the factor of two presented in table 2. The spatial distribution is characterised by one dominant patch of each positive and negative values of  $\tau_L$ , the maximum of both being located on the  $(x, y)$  symmetry plane, the former (positive) near the particle top, the latter (negative) shifted upstream by approximately  $45^\circ$  ( $30^\circ$ ) in case F10 (F50). From the contours, it appears that the flow below the virtual wall contributes little to the lift.

In order to quantify the contribution integrated from the bottom of a particle up to a certain fraction of its diameter, we can define a cumulative function

$$\mathcal{S}_\phi(y) = \frac{D}{2} \int_0^y \int_0^{2\pi} \tau_\phi(y, \theta) \, d\theta dy, \quad (9)$$

where  $\tau_\phi(y, \theta)$  stands for either  $\tau_L$  or  $\tau_D$  evaluated at a position on the sphere’s surface given by the wall-distance  $y$  and an azimuthal angle  $\theta$  in the wall-parallel plane. Figure 12 shows  $\mathcal{S}_L$  and  $\mathcal{S}_D$  normalised by the net values of lift and drag, respectively. The contribution to the net drag by the flow in the lower half of the sphere is small in both cases, the cumulative drag value increasing monotonically and with increasing slope from the wall to the top of the sphere. Conversely, the cumulative contribution to the lift first increases with increasing wall-distance up to values of approximately 25% (40%) of the total in case F10 (F50) at  $y \approx 0.5D$ , before decreasing again to a small value at  $y \approx 0.9D$ . Beyond that, in a small area surrounding the top of the sphere, is where most of the net lift is generated. In case F50, the lift increases with respect to case F10 more than the drag, which leads to a higher angle,  $\alpha = \arctan(C_F^y/C_F^x)$ , of the resulting force (cf. table 2).

The spanwise force should be zero for symmetry reasons. In both cases the calculated mean spanwise force coefficient is more than two orders of magnitude lower than the drag coefficient. This fact provides confidence in the convergence of the statistics.

Additional support to the mean forces just discussed is provided by comparison to experimental measurements performed in a somewhat similar configuration by Hall (1988). In that study, the mean lift on a particle near a boundary was measured in a wind tunnel with smooth as well as rough walls. The interesting case for the present discussion consisted of a sphere of diameter  $D$  placed in-between spanwise rods of diameter  $D_r$  evenly spaced out with a distance  $D_r$ . Figure 13 presents the comparison of the mean lift normalised by  $\rho\nu^2$  as a function of  $D^+$ , between the values obtained in the experiments of Hall (1988) and the present simulations. In spite of the different setups, the lift obtained in case F10 is perfectly consistent with the measurements while the lift obtained in case F50 is somewhat lower. The reason for this might be that in the setup of the simulations the neighbouring spheres are closer producing an increased sheltering effect. This is also supported by the experimental observation that lower lift values are obtained when the value of  $D_r/D$  is increased (Hall, 1988).

In contrast to the direct relation between the mean flow field and the mean forces on a particle, a similar straightforward relation between the statistics of the fluid velocity fluctuations and of the particle force fluctuations cannot be derived from equation (5). This is due to two factors. First, the definition of the standard deviation (and higher order moments) of the force fluctuations is non-linear. Second, the integrals in equation (5) act like a filter in the sense that not all scales participate in creating force fluctuations on a particle. For example, flow scales much smaller than  $D$  might cancel out in the integral sense as will be discussed in detail in §3.4. In spite of this observation, a direct relation between flow velocity statistics above the bed or behind an obstacle is often assumed in the literature in order to estimate the intensity of force fluctuations on a particle (cf. Papanicolaou *et al.*, 2002; García, 2008).

In the present simulations we observe that the standard deviations for the streamwise and spanwise components of the particle forces are of similar magnitude in both cases F10 and F50

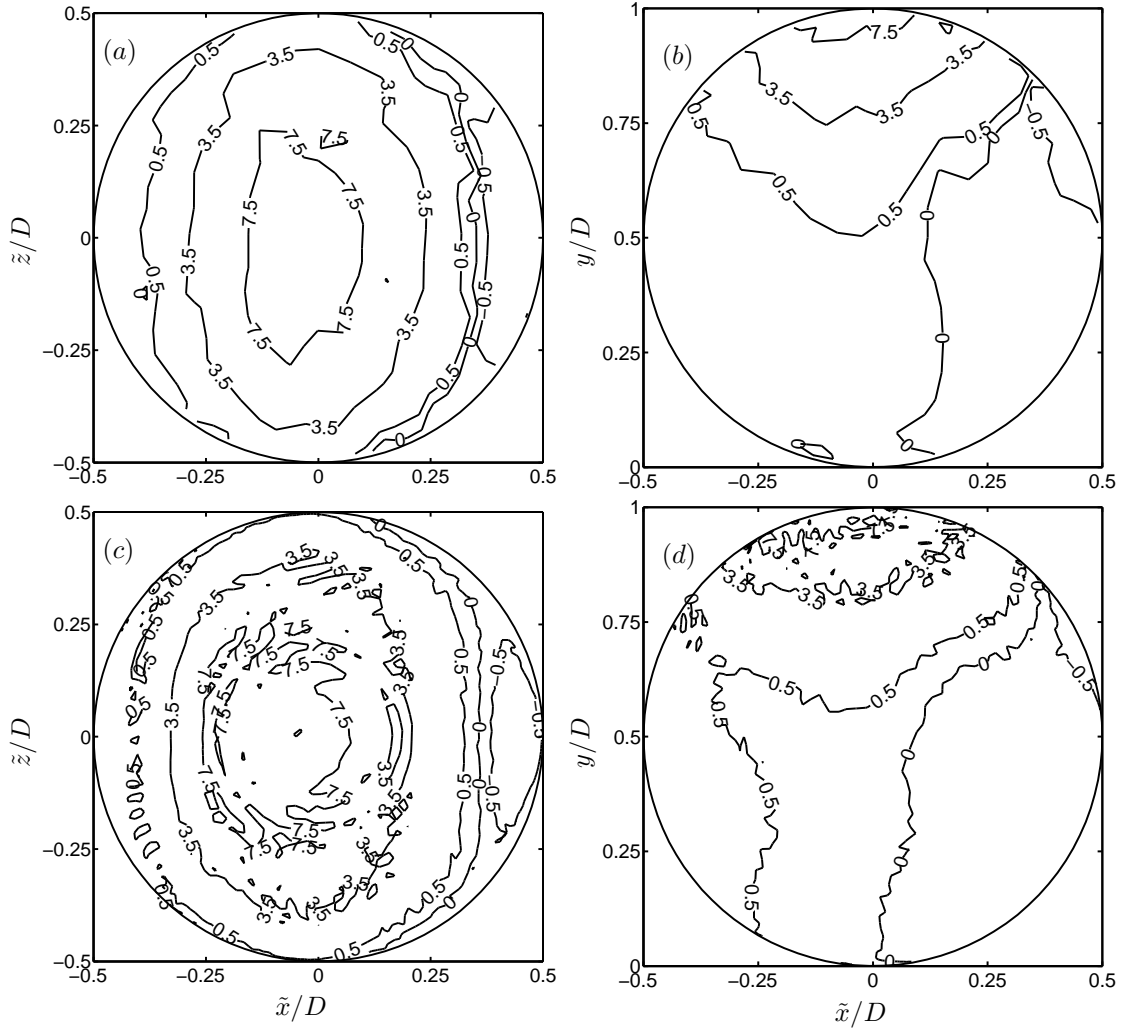


Figure 10: Spatial distribution of  $\tau_D$ , normalised by  $F_R/A_{sph}$ .  $\tilde{x}$  and  $\tilde{z}$  are the coordinates with respect to the particle centre. The contour lines shown correspond to  $[-0.5, 0.0, 0.5, 3.5, 7.5]$ ; Panels (a) and (b) show case F10, panels (c) and (d) show case F50.



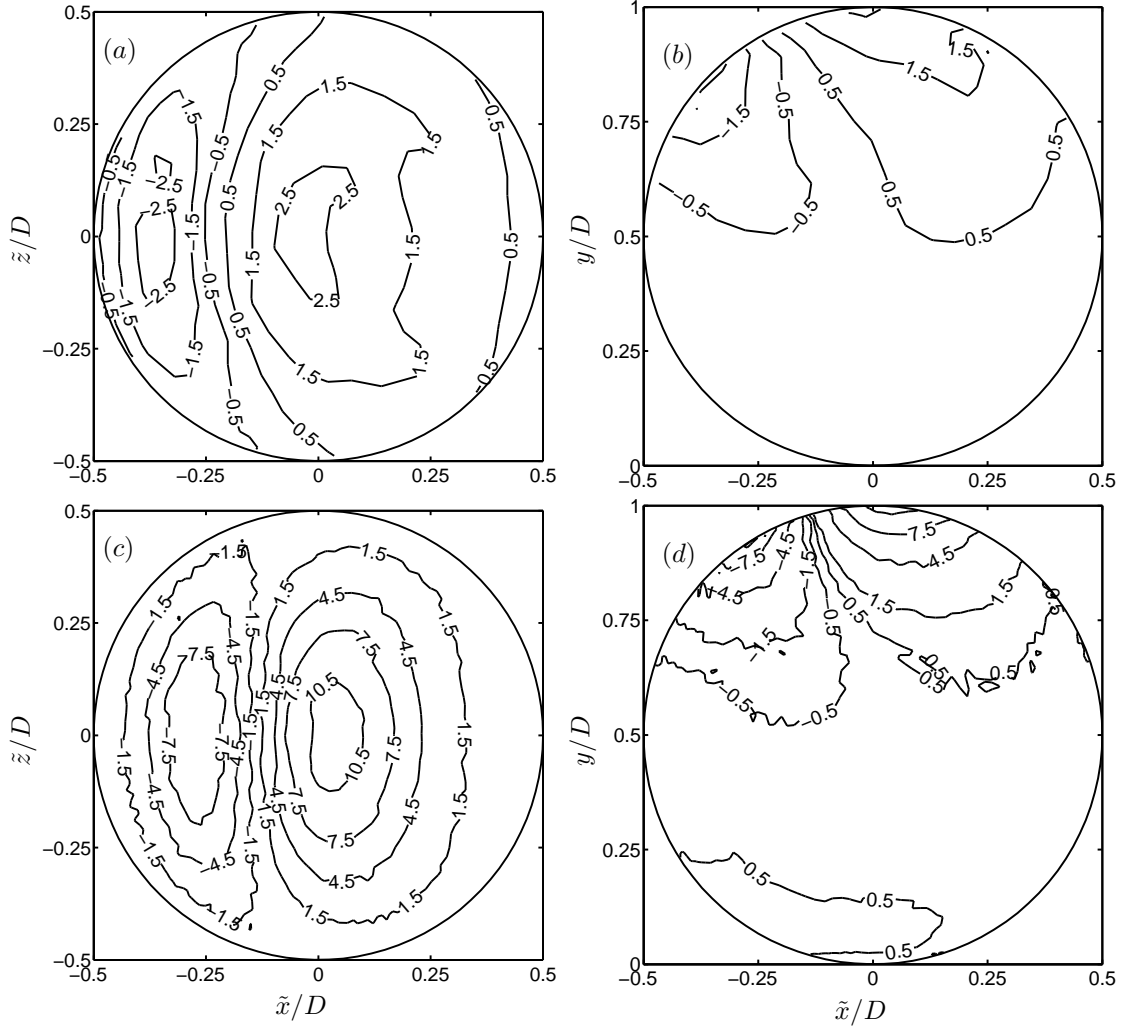


Figure 11: As figure 10, but for  $\tau_L$ . The contours lines shown in (a) and (b) are at values from -2.5 to 2.5 in steps of 1, in (c) and (d) at values from -7.5 to 10.5 in steps of 3; in (d) additionally the contours at the values -0.5 and 0.5 are shown.

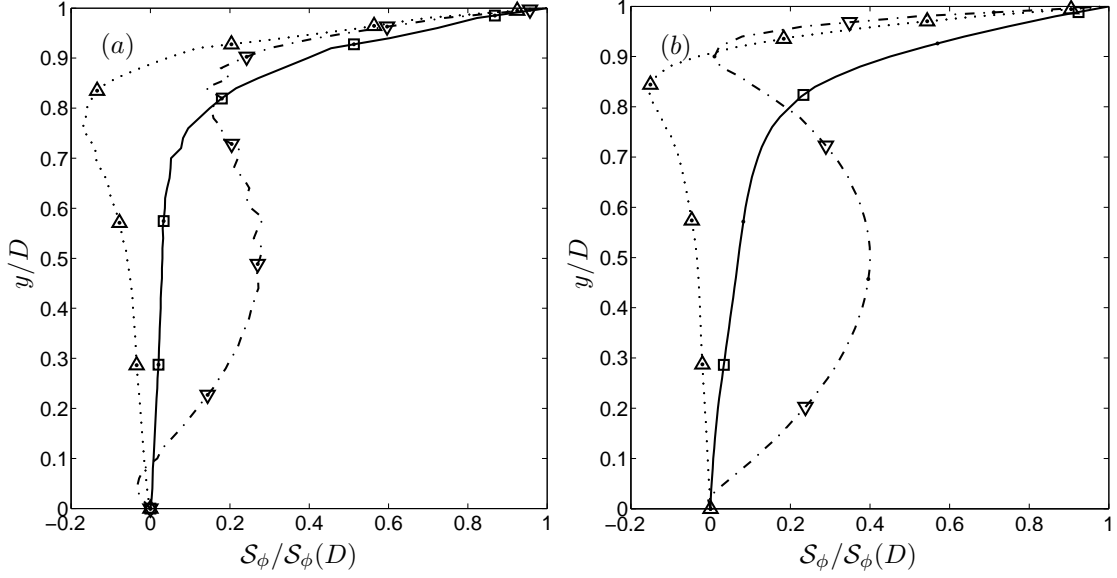


Figure 12: Cumulative function  $\mathcal{S}_\phi$  of the stress contribution to the mean value of drag, lift and spanwise torque on a particle as a function of  $y$  and normalised by its maximum value.  $-\square-$ , drag;  $-\cdot-\nabla-\cdot-$ , lift;  $\cdots\triangle\cdots$ , spanwise torque. Panel (a) shows case F10, panel (b) shows case F50.

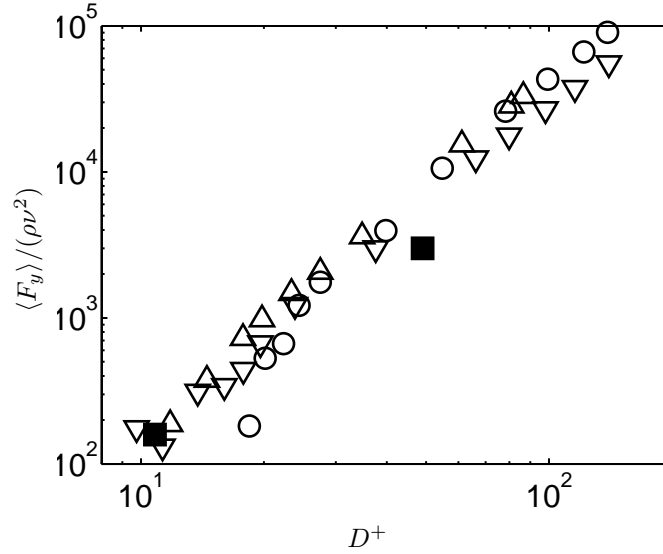


Figure 13: Comparison of  $\langle F_y \rangle / (\rho \nu^2)$  as a function of  $D^+$  of case F10 and case F50 (solid symbols) with mean lift on a sphere placed in between roughness elements in a boundary layer by Hall (1988) (open symbols); present simulations:  $\blacksquare$ ; experiments Hall (1988):  $\nabla$ :  $D_r = 5/3D$ ,  $\circ$ :  $D_r = D$ ,  $\triangleleft$ :  $D_r = 2/3D$ , where  $D_r$  is the radius of the rods spaced with  $D_r$  upstream and downstream of the sphere.

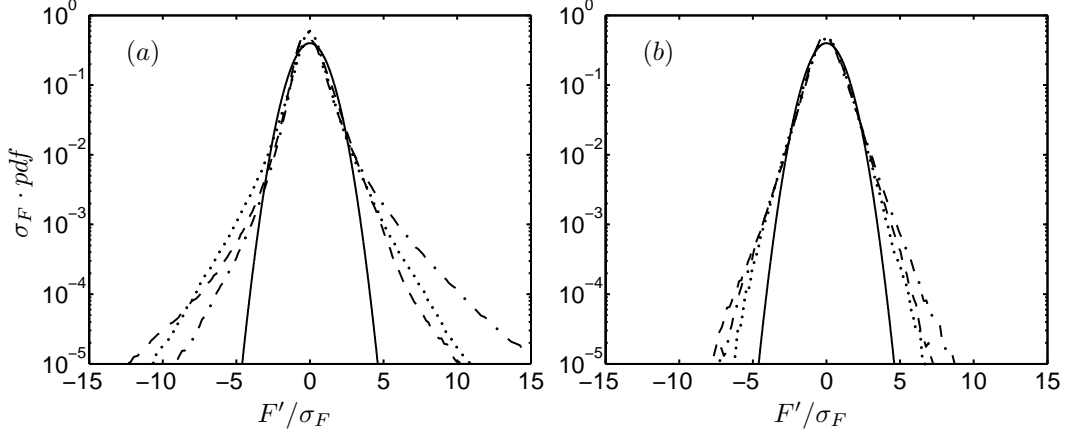


Figure 14: Normalised probability density functions of force fluctuations. (a): case F10; (b): case F50; continuous line: Gaussian distribution, dashed line:  $F'_x/\sigma_F^x$ ; dash-dotted line:  $F'_y/\sigma_F^y$ ; dotted line:  $F'_z/\sigma_F^z$ .

(cf. table 2). It is also found that the standard deviation of lift in both cases is roughly half the value of the other two components. Overall the intensity of the fluctuations in case F50 is more than a factor of two larger than in case F10. Thus, the particle force fluctuations in the present case do not seem to scale directly with the intensity of the plane- and time-averaged fluid velocity fluctuations (cf. figure 4), since  $u_{rms}$  is larger than  $w_{rms}$  over most of the flow depth, and especially close to the wall. Furthermore, the difference in the fluid velocity fluctuation intensities between case F10 and F50 is very small compared to the above stated difference in the particle force fluctuation intensities. It can therefore be concluded that a direct link between fluid and particle force fluctuation intensities cannot be inferred in the present cases.

The results of skewness and kurtosis of the force distributions (cf. table 2) are now discussed jointly with the probability density function (pdf) of the particle force fluctuations shown in figure 14. For both cases F10 and F50 the highest skewness is obtained for the lift, i.e.  $S_F^y$ . In other words, large positive lift fluctuations are significantly more likely to occur than large negative lift fluctuations. This is clearly visible in figure 14(a), where lift events of several standard deviations higher than the mean have a non-negligible probability of occurrence. In case F50, this effect is not as strong as in case F10 (cf. figure 14b), and accordingly the value of the skewness  $S_F^y$  is lower in the former case. The small positive skewness of the drag indicates similarly that instantaneous high drag events are more likely compared to low drag events. For this component, however, the effect appears to be much weaker as compared to lift. Finally, symmetry arguments again lead to the conclusion that  $S_F^z$  should be zero, and this is indeed the case.

The kurtosis of all profiles is rather large indicating a strong intermittency of the forces, i.e. the pdfs in figure 14 exhibit much longer tails than a Gaussian distribution. However, as the spheres become larger the values of skewness and kurtosis approach the Gaussian values of zero and three. This trend might be due to the fact that the force on the particle is an integral quantity, and as mentioned before, small intermittent events might be averaged out. This argument is further elaborated in §3.4 below.

The present results might be compared to the experimental data provided by Mollinger & Nieuwstadt (1996) for lift fluctuations on a single sphere with  $D^+ = 2.9$  positioned on top of a smooth wall. Although their flow configuration is somewhat different (no sheltering effect, turbulent boundary layer) they also report positive values for the skewness ( $S_F^y = 1.2$ ) and high values of flatness ( $K_F^y = 7.0$ ). Furthermore, the pdf of the lift fluctuations in their study is of similar shape to the one obtained in the present case F10. This qualitative agreement suggests that the present results might be relevant to a broader range of flow configurations, e.g. different sphere arrangements or packing densities.

Case	$C_T^x$	$C_T^y$	$C_T^z$	$\sigma_T^x/T_R$	$\sigma_T^y/T_R$	$\sigma_T^z/T_R$	$S_T^x$	$S_T^y$	$S_T^z$	$K_T^x$	$K_T^y$	$K_T^z$
F10	0.00	0.00	-0.98	0.21	0.04	0.36	0.01	-0.01	-1.04	6.46	6.17	4.72
F50	0.00	0.00	-0.73	0.17	0.11	0.27	-0.01	-0.01	-0.76	3.75	4.91	3.37

Table 3: Statistical moments of torque on particles in case F10 and F50.  $C_T^{x_i} = \langle T^{x_i} \rangle / T_R$  is the normalised mean torque component in the  $x_i$ -direction,  $\sigma_T^{x_i}$  is the standard deviation of the torque in  $x_i$  direction,  $S_T^{x_i}$  and  $K_T^{x_i}$  are the skewness and kurtosis of the respective torque component.

### 3.4 Statistics of particle torque

The hydrodynamic torque  $\mathbf{T}$  acting on a spherical particle with respect to its centre is defined as follows:

$$\mathbf{T} = \int_{\Gamma} \mathbf{r}_c \times (\boldsymbol{\tau} \cdot \mathbf{n}) \, d\Gamma, \quad (10)$$

where  $\mathbf{r}_c = (x_c, y_c, z_c)$  is the distance vector from the particle centre to an element of the surface  $\Gamma$ . It should be noted that – contrary to the definition of the total particle force (5) – the pressure does not enter the integral (10), since in the present case the differential pressure force  $-p^{tot} \mathbf{n} ds$  acting on a surface element  $ds$ , is always directed towards the particle centre. Based on the reference force  $F_R$  given in §3.3 the reference torque is defined as  $T_R = F_R r_R$ , where  $r_R$  is the distance from the particle centre to the virtual wall,  $r_R = y_0 - D/2$ . The quantity  $T_R$  will be used in the following for the normalisation of the various torque-related statistical values. A sketch that illustrates the definition of the torque on a particle can be seen in figure 9(a).

Table 3 shows the statistical moments of the torque acting on the particles. Here  $C_T^{x_i}$  is the mean torque in the  $x_i$ -direction normalised by  $T_R$ . Once more, due to symmetry the only non-zero component of the mean torque is expected to be  $C_T^z$ . The table shows that negative mean values for the spanwise component are obtained. These negative values of  $C_T^z$  are expected for the torque on a particle in positive shear (cf. figure 2 and figure 6). The torque coefficient as it is defined above takes values close to  $-1$  for case F10, while it is approximately 25% lower in magnitude in case F50.

In order to analyse these integral results in more detail figure 15 shows the distribution on the sphere’s surface of the stresses leading to spanwise torque,

$$\tau_T = \tau_L x_c - \tau_D y_c. \quad (11)$$

The distribution of  $\tau_T$  in figure 15 is in both cases similar in shape and values of the contours. As for the distribution of  $\tau_D$  (cf. figure 10), a shift towards the particle front can be observed for the minimum values of  $\tau_T$  near the particle top. This shift is more pronounced in case F50. Negative values of  $\tau_T$  occur almost exclusively in the upper part of the particle. Thus over most part of the sphere  $\tau_T$  is positive, but low in magnitude. The cumulative contribution function of  $\tau_T$ , denoted by  $\mathcal{S}_T$  (cf. equation 9), which is also shown in figure 12, reveals that when integrating the contribution of  $\tau_T$  in the lower part of the sphere it adds up to approximately  $-0.15 C_T^z$  in the vicinity of the virtual wall. In both cases the values of  $\tau_T$  are predominantly negative for wall-distances above  $y \approx 0.8D$ , such that  $\mathcal{S}_T$  vanishes around  $y = 0.9D$ . It can therefore be argued that the net spanwise torque  $C_T^z$  is generated in the surface area between a wall distance of  $y = 0.9D$  and the particle top (i.e. the region highlighted by a dashed line in figure 15).

Before turning to the discussion of the torque fluctuations, first a simple model is introduced, which allows us to elucidate some of the characteristics of the torque fluctuations by considering the scales of flow motion that lead to the generation of torque on a particle. It should be noted that other authors have previously investigated the relation between flow structures at different scales and the forces/torque exerted upon sediment particles (e.g. Hofland, 2005). Here we employ a somewhat different approach which allows us to use data from a smooth-wall flow. In particular, we first analyse drag and torque fluctuations experienced by a square wall-element in channel flow

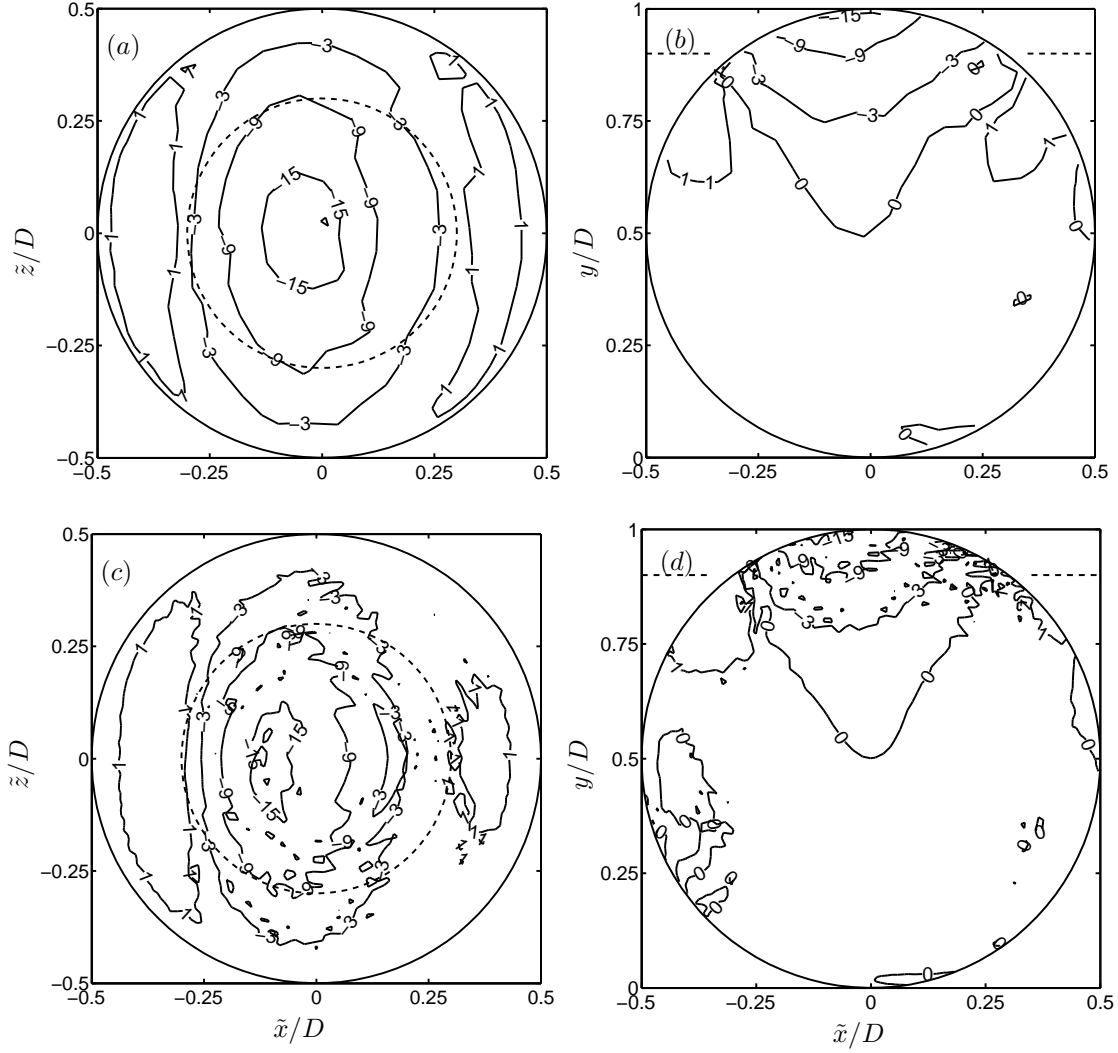


Figure 15: Spatial distribution of  $\tau_T$ , normalised by  $T_R/A_{sph}$ ;  $\tilde{x}$  and  $\tilde{z}$  are the coordinates with respect to the particle centre. Contour lines are shown at values of  $[-15, -9, -3, 1]$  in all plots; in (b) and (d) additionally the contour line at zero value is shown. The dashed line indicates the location of  $y = 0.9D$ . Panels (a) and (b) show case F10, panels (c) and (d) show case F50.

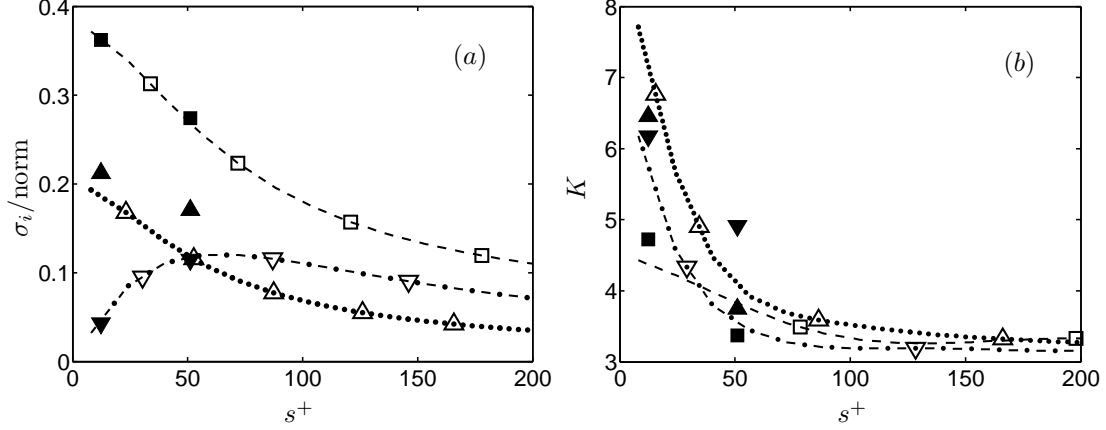


Figure 16: Statistical moments (*a* showing the root-mean-square value, *b* the kurtosis) of force and torque obtained from the simple model described in the text and of actual values of the corresponding torque obtained on the particles in case F10 and F50. In the former case (smooth wall) the integration is performed over a square wall element of side length  $s$ , the open symbols and lines corresponding to:  $-\square-$ ,  $\mathcal{F}_x$ ;  $-\nabla-$ ,  $\mathcal{T}_y$ ;  $\cdots\triangle\cdots$ ,  $\mathcal{F}_z$ . The forces are normalised by  $\rho u_\tau^2 s^2$ , torque is normalised by  $1/2 \rho u_\tau^2 s^3$ . In the latter case (rough wall) the integration is taken over the particle surface (as given in equation 10) with the filled symbols corresponding to:  $\blacktriangle$ ,  $T_x$ ;  $\blacktriangledown$ ,  $T_y$ ;  $\blacksquare$ ,  $T_z$ . Note that in cases F10 and F50 the reference length  $s$  is taken as  $\sqrt{A_R}$ .

with a geometrically smooth wall, systematically varying the linear dimension of the wall-element. Subsequently, the obtained statistical results are related to the corresponding statistics of the components of the torque acting on a spherical particle in our main simulations.

Analogously to the definition of force and torque on a particle the force in the  $x$  and  $z$  direction on a square surface element in a smooth-wall channel with area  $A_s = s^2$  can be defined as

$$\mathcal{F}_x = \int_{-s/2}^{+s/2} \int_{-s/2}^{+s/2} \tau_{xy}|_{y=0} \, dx dz, \quad \mathcal{F}_z = \int_{-s/2}^{+s/2} \int_{-s/2}^{+s/2} \tau_{zy}|_{y=0} \, dx dz, \quad (12)$$

where  $s$  is the side length of the element and  $\tau_{ij}|_{y=0}$  are the components of the stress tensor at the wall. The torque on the element with respect to its centre can be defined as

$$\mathcal{T}_y = \int_{-s/2}^{s/2} \int_{-s/2}^{s/2} \left( r_x^s \tau_{zy}|_{y=0} - r_z^s \tau_{xy}|_{y=0} \right) \, dx dz, \quad (13)$$

where  $\mathbf{r}^s$  is the direction vector with respect to the centre of the area element. A sketch that illustrates the definition of the force and torque on a square element in a smooth-wall channel can be seen in figure 9(b).

Drag and spanwise force on the smooth-wall element are expected to be mostly affected by velocity scales in streamwise and spanwise direction, respectively, that are of sizes similar or larger than  $s$ . The effect of velocity fluctuations at length scales much smaller than  $s$  will tend to cancel out due to the integral character of the force (12). Thus the highest value of force fluctuation should be expected for smallest values of  $s$ , as the contribution of the smaller scales is lost for larger values of  $s$ . Conversely, due to the cross-product in (13) the torque on a smooth-wall surface element is mostly affected by wall normal vortical motions of sizes comparable to  $s$ . The effect of much smaller and much larger scales will cancel out or lead to only small values of torque. Thus for small as well as high values of  $s$  small values of  $\mathcal{T}_y$  are expected. At some intermediate value of  $s$ , the characteristics of wall normal vortical motions should be most efficient in generating torque, leading to maximum values of  $\mathcal{T}_y$ . Figure 16(a) supports that hypothesis. It shows the normalised standard deviation of the forces and torque on the surface element,  $\sigma_{\mathcal{F}}^x$ ,  $\sigma_{\mathcal{F}}^z$  and  $\sigma_{\mathcal{T}}^y$  normalised by

$\rho u_\tau^2 s^2$  and  $1/2 \rho u_\tau^2 s^3$ , respectively. On a square element with  $s^+ \approx 70$  torque appears to be most efficiently produced. This value is somewhat larger than the average distance between the low speed and high speed streak close to the wall which is commonly found to be of order  $50\nu/u_\tau$ . As can be seen in figure 16(b) the kurtosis of the above quantities monotonically decreases with the size of the surface element indicating that the intermittency of the small scales is larger than that of the large scales.

A direct analogy between this smooth-wall model and the force and torque on a particle is not fully justified, as the flow and the geometry are more complex in the present case. However, some of the characteristics of the particle torque statistics obtained for the present cases can be explained with the aid of such a simple model as will be discussed in the following. Please note that only one torque component can be defined for a plane wall element (here  $\mathcal{T}_y$ ), in addition to the two in-plane forces considered ( $\mathcal{F}_x$  and  $\mathcal{F}_z$ ). A correspondence with the three torque components acting on a spherical particle is established when considering the plane wall element as being located at the top (i.e. the pole located at  $y = D$ ) of the particles in case F10 and F50. The componentwise correspondence is then:  $\mathcal{F}_x \rightarrow -T_z$ ,  $\mathcal{T}_y \rightarrow T_y$ ,  $\mathcal{F}_z \rightarrow -T_x$  (cf. figure 9).

The normalised standard deviations of the particle torque components shown in table 3 are all non-zero as can be expected. The amplitudes of the fluctuations of the streamwise and spanwise torque components are found to be the largest, while the wall-normal component is significantly weaker. Compared to the small-sphere case (F10), the streamwise and spanwise components are smaller in the large sphere case (F50), by 20% ( $\sigma_T^x/T_R$ ) and 25% ( $\sigma_T^z/T_R$ ), respectively. Contrarily, the wall-normal value  $\sigma_T^y/T_R$  is significantly larger in case F50 than in case F10 (nearly by a factor of three).

Figure 16, which has already been partially discussed above, also shows the second and fourth statistical moments of particle torque fluctuations as a function of particle size. As can be seen the standard deviation (figure 16a) of the wall normal torque acting on the particles,  $T_y$ , matches rather well the standard deviation of the wall normal torque exerted on a comparable-size square element in the reference smooth-wall flow,  $\mathcal{T}_y$ . In addition, the figure shows that the standard deviation of the spanwise torque,  $T_z$ , compares very well to the standard deviation of the drag exerted on a square element in the smooth wall case,  $\mathcal{F}_x$ . Concerning the streamwise component of particle torque,  $T_x$ , it is found that its standard deviation is somewhat larger than the standard deviation of the spanwise force fluctuations in the smooth wall model,  $\mathcal{F}_z$ ; however, both exhibit a similar decreasing trend with increasing values of the length scale. The overall good agreement between fluctuation intensity of forces/torque acting on an element of a smooth wall and the corresponding torque components of the particle in case F10 and case F50 is interesting for several reasons. First, it suggests that the significant torque fluctuations are generated in a rather limited region around the particle tops where apparently to some extent the analogy with the hydrodynamic action on a wall-parallel square element holds. In particular, the present simulations F10 and F50 provide two data points in the hydraulically smooth and transitionally rough flow regime, which are fully consistent with the existence of a length scale/particle size of maximum wall-normal torque generation, as suggested by the simplified model. Secondly, if the above analogy is accepted, then it implies that the response of the particle torque fluctuations to the near-wall turbulent flow can indeed be described as a selective filtering effect, mainly characterised by a single length scale (the particle diameter).

Normalised pdfs of the particle torque fluctuations are shown in figure 17. It can be seen that the curves for all three torque components in both cases F10 and F50 approximately match the curves of the corresponding force/torque components of the smooth-wall model (evaluated with a side-length  $s$  matching the respective length  $\sqrt{A_R}$ ), thereby further corroborating the analogy. Concerning the shape of the particle torque pdfs themselves, it is observed that the two symmetric components (streamwise  $T_x$  and wall-normal  $T_y$ ) have significantly longer tails than a Gaussian function, and consequently exhibit higher than Gaussian values of kurtosis (cf. table 3). The kurtosis is found to decrease with increasing particle size, consistent with the above filtering argument (also cf. figure 12b).

The pdf of the fluctuations of the spanwise component of particle torque,  $T_z$ , is clearly asymmetric with a pronounced negative skewness. Now, it is well established that the pdf of stream-

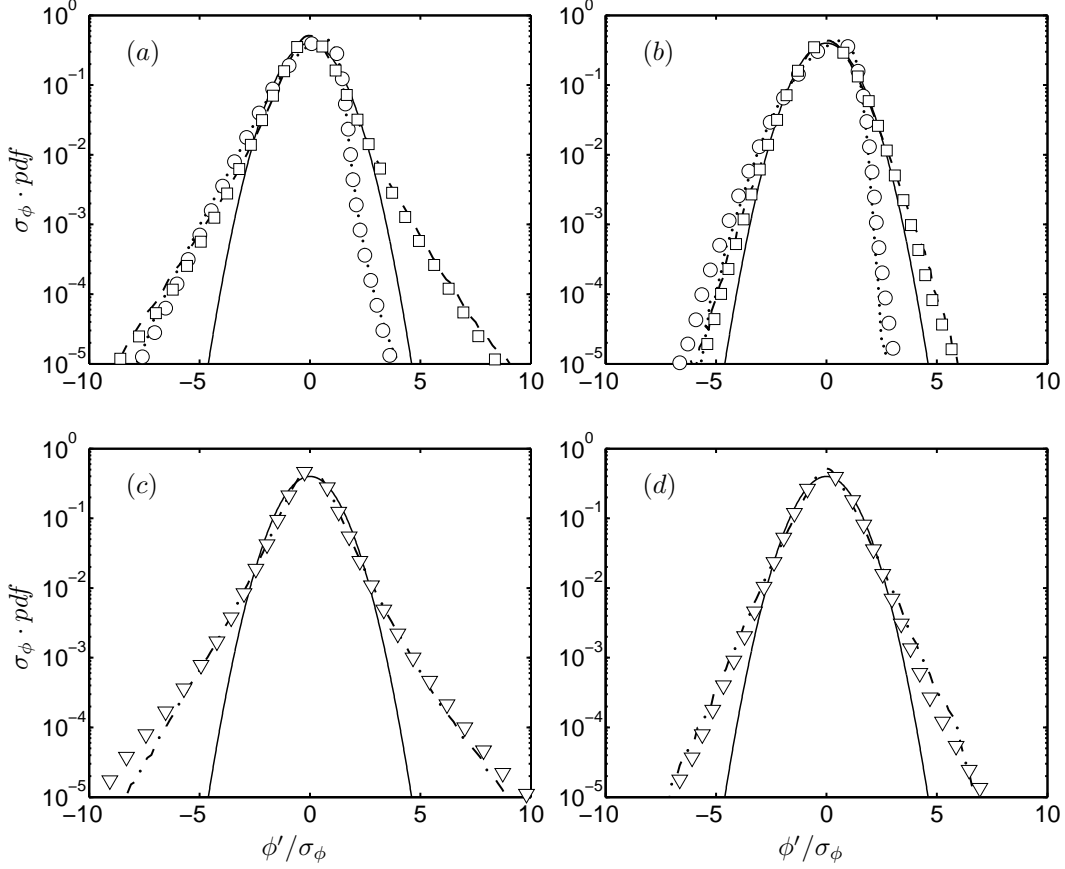


Figure 17: Normalised pdfs of the quantities for which statistical moments have been shown in figure 16. The panels (a) and (c) show data from case F10 compared to data from the simple model with  $s^+ = 12$ ; panels (b) and (d) show data from case F50 compared to data from the simple model with  $s^+ = 52$ . In Panels (a) and (b) the lines and symbols correspond to: dashed line,  $T'_x/\sigma_T^x$ ; dotted line,  $T'_z/\sigma_T^z$ ;  $\circ$ ,  $-\mathcal{F}'_x/\sigma_{\mathcal{F}}^x$ ;  $\square$ ,  $-\mathcal{F}'_z/\sigma_{\mathcal{F}}^z$  (please note the negative signs). Panels (c) and (d) show: dash-dotted line,  $T'_y/\sigma_T^y$ ;  $\nabla$ ,  $\mathcal{T}'_y/\sigma_{\mathcal{T}}^y$ . The solid line corresponds to a Gaussian distribution.

wise velocity fluctuations  $u'$  in smooth-wall channel flow is positively skewed close to the wall (Kim *et al.*, 1987; Jiménez & Hoyas, 2008). In the limit of a wall-element with vanishing size, the pdf of  $\mathcal{F}_x$  is directly related to the pdf of the streamwise velocity fluctuations just above the wall. Since, as found above, the particle torque component  $T_z$  behaves similarly as the smooth-wall force  $-\mathcal{F}_x$  (note the changed sign), the observed negative skewness of the former is consistent with the positively skewed streamwise velocity pdf previously found in smooth-wall channel flow.

It should be noted that the analogy drawn between shear forces acting upon a square element of a smooth-wall channel flow and the corresponding hydrodynamic torque components of spherical particles in the roughness layer can be expected to lose its appeal in the fully rough regime. In that case, which is outside the scope of the present study, pressure-induced forces will by far outweigh viscous forces. Although the torque around the particle center will still by definition be devoid of a pressure contribution (10), other quantities of interest to the onset of particle motion, such as the torque around the line connecting the contact points with the downstream neighbor particles, might be dominated by the contribution from pressure forces. Therefore, the main utility of the proposed simple model is presumably limited to the regime of transitional roughness.



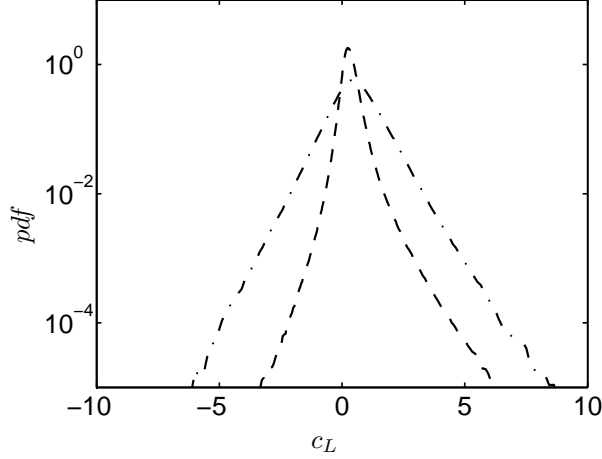


Figure 18: Non-normalized pdf of the lift coefficient defined as  $c_L = F_y/(\rho u_\tau^2 D^2 \pi/4)$ , dashed line: case F10, dash-dotted line: case F50.

### 3.5 Implications for the onset of sediment erosion

Sediment erosion is often parametrised in terms of the non-dimensional Shields number  $\theta$  which is defined as follows:

$$\theta = \frac{\tau_w}{(\rho_p - \rho) g D}, \quad (14)$$

where  $\tau_w = \rho u_\tau^2$  is the wall shear-stress,  $\rho_p$  the density of the sediment particles and  $g$  the value of the gravitational acceleration (Shields, 1936; van Rijn, 1993; García, 2008). If we suppose that erosion is initiated by lift forces alone, then we can characterise the onset of erosion by a balance between hydrodynamic lift force,  $F_y$ , and buoyant weight of the particle,  $F_B = (\rho_p - \rho) g D^3 \pi/6$ , yielding the following expression for the critical Shields parameter:

$$\theta_c = \frac{2}{3c_L}, \quad (15)$$

where the lift coefficient is defined as  $c_L = F_y/(\rho u_\tau^2 D^2 \pi/4)$ . Please note, that in the above definition of  $c_L$  a slightly different normalisation than in §3.3 is chosen. It can be seen that for this erosion scenario the critical value of the Shields number is inversely proportional to the lift coefficient at the onset of erosion.

Figure 18 shows the pdf of the lift coefficient  $c_L$  for the two present cases. In order to determine the smallest value of the Shields parameter for which sediment erosion can be initiated, the largest occurring value of  $c_L$  needs to be considered in each case. Since the pdfs exhibit exponential tails, it is difficult to determine a precise upper bound of  $c_L$ . However, when a given (small) minimum probability of observation is fixed, it is clear that the larger spheres (case F50) will yield a larger maximum value of  $c_L$  than the smaller spheres (F10). Consequently, a smaller critical Shields number is obtained for the spheres in case F50. Other modes of erosion (sliding parallel to the contact point with the downstream neighbour particles; rotation around the contact point) have also been analysed with similar conclusions (graphs of pdfs omitted).

Although exhibiting considerable scatter, experiments and field observations seem to indicate an increase with  $D^+$  of the critical Shields number  $\theta_c$  over the current range of particle diameters (van Rijn, 1993; García, 2008). One has to be cautious, however, since results obtained in our idealised flow configuration are compared to experimental observations in flows involving a wide range of different irregular particle arrangements as well as varying particle shapes and size distributions. With this caveat in mind, we can take the different trend found in the present simulations ( $\theta_c$  decreases from  $D^+ = 10$  to  $D^+ = 50$ ) as compared to experiments ( $\theta_c$  increases from  $D^+ \approx 10$

to  $D^+ \approx 100$ ) as an indication that extreme force- and torque-generating events recorded in fixed-particle configurations might not immediately yield a criterion which is sufficient to judge whether erosion will indeed occur as predicted when particles are freely mobile (under otherwise identical conditions). In particular, the question of the influence of the interaction between the incipient particle motion and the surrounding flow field as well as the related question of the necessary duration of force-/torque-generating flow events cannot be answered with certainty based upon fixed-particle data alone. In order to answer these queries, additional studies involving an analysis of high-fidelity data of the actual process of sediment erosion need to be carried out.

## 4 Summary and conclusions

Direct numerical simulation of open channel flow over a geometrically rough wall has been performed at a bulk Reynolds number of  $Re_b \approx 2900$ . The wall consisted of a layer of spheres in a square arrangement touching a solid wall. Two particle diameters were considered: case F10 with  $D^+ = 10.7$  ( $Re_\tau = 188$ ), and case F50 with  $D^+ = 49.3$  ( $Re_\tau = 235$ ). In case F10 the effect of roughness on the flow field statistics was small, and the limit of the hydraulically smooth flow regime is approached; in case F50 the roughness effect was stronger, and the flow is in the transitionally rough flow regime.

The complexity of the time-averaged three-dimensional flow field within the roughness layer was discussed in detail. In both cases a recirculation forms downstream of the spheres that is connected over the entire spanwise direction, being more pronounced in the large sphere case. Three-dimensionality above the roughness layer is lost rapidly with wall-distance, yielding a time averaged flow field which is essentially one-dimensional beyond a distance of two particle diameters.

The main result of this paper is the characterisation of the force and torque acting on a particle due to the turbulent flow. It was found that in the present cases the mean drag on a sphere is 4% (case F10) and 15% (case F50) higher than the reference force  $F_R = \rho u_\tau^2 A_R$ , where  $A_R$  is the wall-normal projected area of the wall per particle. Given our definition of the friction velocity, these numbers reflect the fact that the drag force on the roughened bottom wall (below the fixed spheres) is small. In both cases a strong positive lift was obtained in agreement with previous experiments, exceeding values of 18% and 32%, respectively, of the corresponding drag. The values of the mean spanwise torque on a particle are comparable to  $-F_R r_R$ , where  $r_R$  is the distance from the particle centre to the position of the virtual wall, located at a distance of  $y_0 = 0.8D$  from the plane part of the solid wall. It was shown that in both cases the mean drag, lift and spanwise torque are to a large extent produced in a region of the particle surface which is located above the virtual wall ( $y > y_0$ ). The spatial distribution over the particle surface of the stresses that lead to time-averaged drag, lift and spanwise torque are found to be similar in shape in the two cases.

We have observed that the intensity of particle force fluctuations (when normalised by  $F_R$ ) is significantly larger in the large-sphere case. Conversely, when analysing the torque it is found that only the fluctuation intensity of the spanwise component is larger in the large-sphere case, whereas the two remaining components exhibit smaller fluctuation intensities when the sphere is larger. By means of a simplified model we were able to show that the torque fluctuations might be explained by the spheres acting as a filter with respect to the size of the flow scales which can effectively generate torque fluctuations. As a model we have considered the shear-forces and torque exerted by the flow on a square wall-element in a smooth-wall configuration. By systematically varying the linear dimension of the wall-element we are able to analyse the influence of the length scale. Here we find that the normalised fluctuation intensity of the streamwise and spanwise shear-forces monotonously decreases with the filter size, while the wall-normal torque experiences a maximum of normalised fluctuation intensity for intermediate filter sizes of approximately 70 wall units. By assuming that the largest part of the particle torque fluctuations is generated in a small area around the particle tops, the results from the simplified model carry over to the corresponding components of the particle torque. We obtain indeed a reasonable agreement between standard deviation and kurtosis of shear-forces and torque acting on a square wall-element on the one hand and respective particle torque components on the other hand. However, since we have only

considered two particle sizes, we cannot state with certainty that wall-normal particle torque fluctuations are indeed most intense at the above mentioned scale of 70 wall units. Similarly, based on the current data it is not possible to judge whether the model is capable of providing insight in the fully rough flow regime. These points should be clarified in future studies.

Fluctuations of both force and torque were found to exhibit strongly non-Gaussian pdfs with particularly long tails. The deviation from a Gaussian distribution was significantly smaller in the large-sphere case, which was attributed to the smaller effect that highly intermittent small scales have on the larger particle surface area. Moreover, it was observed that the spanwise torque component has a marked negative skewness. In the light of the analogy with a wall-element in a smooth-wall configuration, this finding is consistent with the positive skewness of the streamwise velocity fluctuations near the wall in a smooth wall channel flow.

Concerning the potential for sediment erosion, it was concluded from the present data that the largest recorded values of hydrodynamic lift lead to critical Shields numbers which are smaller in the large-sphere case as compared to the small-sphere case. The same trend was found when considering the forces projected onto the direction tangential to the downstream contact point between spheres in neighbouring positions as well as when evaluating the balance of angular moments around the contact point. Measurements in experiments with truly mobile particles seem to indicate the opposite trend (increasing critical Shields number with increasing particle size in the range of  $D^+ \approx 10$  to 100). However, these opposite trends do not necessarily imply a contradiction, since additional effects which might play a role in the dynamical process of erosion have not been addressed in the present study.

Two important idealisations with respect to real-world sediment erosion have been made in the present work: the regularity of the geometrical arrangement and the immobility of the particles. Concerning the geometry, it is expected that different particle arrangements, size distributions and shapes will lead to a modification of the forces acting upon sediment particles. In particular, varying the protrusion of individual particles has been shown to have a significant effect on the onset of erosion (Fenton & Abbott, 1977; Cameron, 2006). In this respect, the configuration studied in the present work can be considered as a case where mutual sheltering of particles is high due to their uniform diameter, spherical shape and regular arrangement.

Concerning the immobility of the particles, we see several consequences arising from this idealisation which could potentially affect the implications for sediment erosion: (i) the modification of the flow field by the particles during the incipient motion; (ii) the determination of the temporal duration of force- and torque-generating flow events which is necessary in order to achieve irreversible onset of particle motion; (iii) the influence of collective mobility. In order to evaluate the importance of these mobility effects, additional data from configurations with truly eroding particles needs to be analysed. It might then still be possible to devise a refined erosion criterion which allows for the determination of erosion probabilities based upon data from fixed-particle configurations.

Both of these additional aspects (the bed geometry and the particle mobility) should be addressed in future studies.

This work was supported by the German Research Foundation (DFG) under project JI 18/19-1. The computations have been carried out at the Steinbuch Centre for Computing (SCC) of Karlsruhe Institute of Technology and at the Leibniz Supercomputing Centre (LRZ) of the Bavarian Academy of Sciences and Humanities. The support from these institutions is gratefully acknowledged. We also thank the anonymous referees for useful suggestions leading to the improvement of the manuscript.

## A The position of the virtual wall and the friction velocity

Several common methods exist for the definition of an origin  $y_0$  of the wall-normal coordinate when analysing turbulent flow statistics over rough walls.

A priori definitions can be based on geometrical considerations. Examples are the volume of the roughness elements divided by the area of the virtual wall (cf. Schlichting, 1936), which for the

present geometry leads to  $y_0/D = 0.44$  (0.56) in case F10 (F50), or the average of the maximum surface elevation, which leads to  $y_0/D = 0.54$  (0.65) in case F10 (F50). A posteriori methods employ the data from measurements or simulations to define  $y_0$ . Thom (1971) and Jackson (1981) propose to define  $y_0$  by the wall-normal position of the centroid of the drag profile on the roughness elements. In the present study such a definition would lead to values of  $y_0/D = 0.88$  (0.84) in case F10 (F50). It should be noted that in case of a porous sediment layer, this definition is biased by the inter-porous flow. Most researchers, however, use methods which involve the adjustment of a logarithmic law to the mean velocity profile (Raupach *et al.*, 1991), especially for high Reynolds number flows. Based on these methods, several studies on turbulent flow over spherical roughness (for various Reynolds numbers, particle arrangements and flow geometries) can be found that provide the value of  $y_0$  for a given particle diameter (cf. reviews in Bayazit, 1983; Nezu & Nakagawa, 1993, p. 26; Dittrich, 1998, p. 29; Detert *et al.*, 2010a), including also studies that match well with the present flow conditions (Nakagawa & Nezu, 1977; Grass *et al.*, 1991; Cameron, 2006; Singh *et al.*, 2007). In these studies the virtual wall is positioned at  $y_0/D$  in the interval 0.61 to 0.82. In some studies the virtual wall is defined at the location of the roughness crests (i.e.  $y_0/D = 1$ ) such as in Manes *et al.* (2007).

In the present work we have selected to fix the position of the virtual wall at a given level  $y_0/D = 0.8$  inside the range of values determined in relevant experiments.

Turning now to the definition of the velocity scale  $u_\tau$ , we will discuss three common approaches in the following. Again, a widely used method is to obtain  $u_\tau$  by adjusting a logarithmic law to the mean velocity profile. Assuming the values  $\kappa = 0.40$  and  $y_0/D = 0.80$  for the Kármán constant and the offset of the virtual wall, respectively, a fit over the range  $50\delta_\nu \leq (y - y_0) \leq 0.5h$  yields  $u_\tau/U_{bh} = 0.062$  (0.081) in case F10 (F50). However, it should be recalled that in the present low-Reynolds number flow the limited extent of the logarithmic region makes this approach relatively error-prone.

Alternatively, the global momentum balance can be used in order to relate the driving force (either due to a pressure gradient or gravity) to the different contributions to the drag force generated at the fluid-solid interfaces. While the mean momentum balance is uniquely defined, it does not immediately provide a velocity scale. In some studies the velocity scale is defined from the volumetric force integrated from the virtual wall-distance to the free surface (for example Nakagawa & Nezu, 1977; Detert *et al.*, 2010a), i.e. in our notation  $u_\tau^2 = -\langle dp_l/dx \rangle h/\rho$ . This definition leads to  $u_\tau/U_{bh} = 0.066$  (0.081) in case F10 (F50). Other authors choose to integrate the driving force exclusively over the volume occupied by the fluid (Manes *et al.*, 2011), leading to  $u_\tau^2 A_w = -\langle dp_l/dx \rangle V_f/\rho$  (where  $A_w$  is the area of the wall-parallel cross-section of the considered control volume and  $V_f$  the corresponding volume occupied by the fluid). This latter definition yields  $u_\tau/U_{bh} = 0.066$  (0.081) in case F10 (F50).

Finally, let us consider definitions based on the total shear stress profile. In smooth-wall flow, the total shear stress  $\tau_{tot}$  is linear with wall-distance and the appropriate velocity scale is given by  $u_\tau^2 = \tau_{tot}(0)/\rho$ . In rough-wall flow,  $\tau_{tot}$  in general deviates from a linear relation below the roughness crests which prevents the use of a similar definition, e.g. based upon  $\tau_{tot}(y = y_0)$ . Instead, some researchers propose to determine the velocity scale independently of the position of the virtual wall by using the total shear stress at the roughness crests, i.e.  $u_\tau^2 = \tau_{tot}(y = D)/\rho$  (Pokrajac *et al.*, 2006). This definition leads to values of  $u_\tau/U_{bh} = 0.066$  (0.080) in case F10 (F50). Note that this latter definition makes a direct comparison of different data sets difficult, since the total shear stress profiles  $\tau_{tot}/(\rho u_\tau^2)$  represented as a function of  $(y - y_0)/h$  will in general not collapse. Alternatively,  $u_\tau$  can be computed from the total shear stress extrapolated from the region where it varies linearly (i.e. above the roughness crests) down to the position of the virtual wall, yielding the defining relation

$$\tau_{tot} = \rho u_\tau^2 \left( 1 - \frac{y - y_0}{h} \right), \quad (16)$$

valid for  $y > D$ . This definition leads to  $u_\tau/U_{bh} = 0.066$  (0.082) in case F10 (F50). Incidentally it can be deduced from the global momentum balance that our definition implies  $u_\tau^2 = -\langle dp_l/dx \rangle h/\rho$ ,

i.e. it turns out that the definition of  $u_\tau$  through (16) is equivalent to the above mentioned definition used by Nakagawa & Nezu (1977) and Detert *et al.* (2010a) based upon an integral of the driving force.

## B Details on averaging procedures

In the present paper two definitions have been used for averaging a discrete flow field,  $\phi(i, j, k)$ , in  $x$ - $z$  planes:

$$\langle \phi \rangle_{xz}^A(j) = \frac{1}{N_x N_z} \sum_{i=1}^{N_x} \sum_{k=1}^{N_z} \phi(i, j, k), \quad (17)$$

$$\langle \phi \rangle_{xz}^B(j) = \frac{1}{N_m(j)} \sum_{i=1}^{N_x} \sum_{k=1}^{N_z} \phi(i, j, k) m(i, j, k), \quad (18)$$

where  $N_x$  and  $N_z$  are the number of grid points in  $x$  and  $z$  directions, respectively, and  $m$  is a field that works as a mask for computing the averages. If a given point lies within the fluid domain, at that point  $m = 1$ , otherwise  $m = 0$ .  $N_m(j)$  is the sum of  $m$  over a wall parallel plane at wall-distance  $y_j$ , i.e.  $N_m(j) = \sum_{i=1}^{N_x} \sum_{k=1}^{N_z} m(i, j, k)$ .  $N_m(j)$  equals  $N_x N_z$  above the roughness layer such that both expressions (18) and (17) are equal to each other away from the roughness elements. Within the roughness layer  $N_m(j)$  and thus the number of samples for each wall parallel plane decreases. In the context of the double-averaging methodology these two quantities are generally referred to as superficial and intrinsic spatial average, respectively (cf. Nikora *et al.*, 2007).

Note that the zero velocity condition is forced only at the surface of the particles due to reasons of efficiency (Uhlmann, 2005a). This leads to fictitious non-zero velocities at the grid points that lie within the particles. Fadlun *et al.* (2000) demonstrated that the external flow is essentially unchanged by this procedure which has been confirmed later by Uhlmann (2005a). Since the internal fictitious flow affects the value of  $\langle \phi \rangle_{xz}^A(j)$  (according to 17) in the roughness layer, we present averages computed according to (18) where the flow within the roughness layer is discussed (i.e. figure 5 and figure 8). When focusing upon the flow above the roughness layer (i.e. in figure 2 and figure 4), we choose to present data computed according to (17), because the number of available samples is larger, as explained in § C.

## C Consistency of runtime and a posteriori statistics

For the flow field statistics presented in this paper, two different sets of data have been used. The first set of flow field statistics was collected during the runtime of the simulation employing equation (17). This leads to a number of the order of  $10^{11}$  samples per wall-normal grid point in case F10 and F50, collected over the entire observation interval. The second set of data was obtained from analysing stored snapshots of the flow field of which 90 were used in each case. The latter set has been used to compute some additional statistical quantities not stored during runtime. Since it provides a smaller number of samples (roughly a factor of  $10^3$  less), we will in the following check its consistency with the more complete set accumulated at runtime.

Figure 19 shows for each case the second order moments of the velocity fluctuations obtained at run-time in comparison to the same quantities obtained from the snapshots of the simulations applying the averaging operator as defined in (17). The differences between the two data sets are small, measuring less than  $0.06u_\tau$  ( $0.02u_\tau$ ) in case F10 (F50). Incidentally, it can be seen from the figures that the discrepancy is largest near the open surface. We can therefore conclude, that the data set provided from the 90 stored snapshots is sufficient for the purpose of computing the quantities shown in figure 5, figure 6, figure 7 and figure 8.

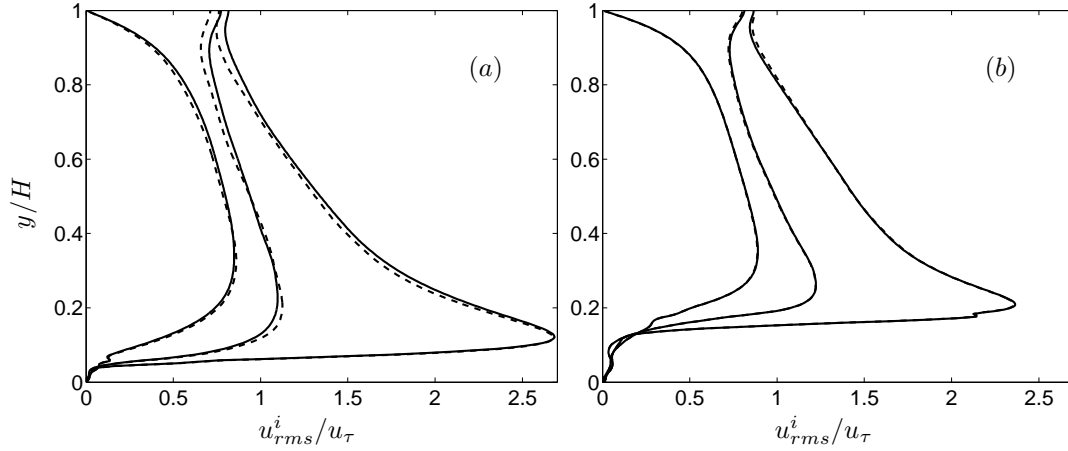


Figure 19: Comparison of velocity fluctuations normalised by  $u_\tau$  obtained from run-time (solid line) and from snapshots (dashed line) as a function of  $y/H$ . Curves from left to right are the components in wall-normal ( $v_{rms}/u_\tau$ ), spanwise ( $w_{rms}/u_\tau$ ) and streamwise ( $u_{rms}/u_\tau$ ) direction. Panel (a) shows case F10, panel (b) shows case F50.

## References

- AUTON, T. 1987 The lift force on a spherical body in a rotational flow. *J. Fluid Mech.* **183**, 199–218.
- AUTON, T. R., HUNT, J. C. R. & PRUD’HOMME, M. 1988 The force on a body in inviscid unsteady non-uniform rotational flow. *J. Fluid Mech.* **197**, 241–257.
- BAGCHI, P. & BALACHANDAR, S. 2002 Steady planar straining flow past a rigid sphere at moderate Reynolds number. *J. Fluid Mech.* **466**, 365–407.
- BAGCHI, P. & BALACHANDAR, S. 2003 Effect of turbulence on the drag and lift of a particle. *Phys. Fluids* **15** (11), 3496–3513.
- BAGCHI, P. & BALACHANDAR, S. 2004 Response of the wake of an isolated particle to an isotropic turbulent flow. *J. Fluid Mech.* **518**, 95–123.
- BAYAZIT, M. 1983 Flow structure and sediment transport mechanics in steep channels. In *Mechanics of Sediment Transport, Proc. EUROMECH 156 Colloquium* (ed. B. M. Sumer & A. Müller), pp. 197–206. A. A. Balkema, Rotterdam, Netherlands.
- BRADSHAW, P. 2000 A note on “critical roughness height” and “transitional roughness”. *Phys. Fluids* **12** (6), 1611–1614.
- CAMERON, S. M. 2006 Near-boundary flow structure and particle entrainment. PhD thesis, University of Auckland.
- COLEBROOK, C. F. 1939 Turbulent flow in pipes with particular reference to the transition region between the smooth- and rough-pipe laws. *J. Inst. Civil Eng.* **11**, 133–56.
- DETERT, M., NIKORA, V. & JIRKA, G. H. 2010a Synoptic velocity and pressure fields at the water-sediment interface of streambeds. *J. Fluid Mech.* **660**, 55–86.
- DETERT, M., WEITBRECHT, V. & JIRKA, G. H. 2010b Laboratory measurements on turbulent pressure fluctuations in and above gravel beds. *J. Hydraul. Eng.* **1**, 126–126.

- DITTRICH, A. 1998 Wechselwirkung Morphologie/ Strömung naturnaher Fließgewässer. Habilitation, Univ. Karlsruhe (TH).
- EINSTEIN, H. A. & EL-SAMNI, E.-S. A. 1949 Hydrodynamic forces on a rough wall. *Rev. Mod. Phys.* **21** (3), 520–524.
- FADLUN, E. A., VERZICCO, R., ORLANDI, P. & MOHD-YUSOF, J. 2000 Combined immersed-boundary finite-difference methods for three-dimensional complex flow simulations. *J. Comput. Phys.* **161** (1), 35 – 60.
- FENTON, J. & ABBOTT, J. 1977 Initial movement of grains on a stream bed: The effect of relative protrusion. *Proc. R. Soc. Lond. A* **352** (1671), 523–537.
- FLORES, O. & JIMÉNEZ, J. 2006 Effect of wall-boundary disturbances on turbulent channel flows. *J. Fluid Mech.* **566**, 357–376.
- GARCÍA, M. H. 2008 *Sedimentation engineering: processes, measurements, modeling, and practice*. American Soc. Civil Eng. (ASCE), Reston, Va., ASCE Manual of Practice 110.
- MUÑOZ GOMA, R. J. & GELHAR, L. W. 1968 Turbulent pipe flow with rough and porous walls. Int. Rep. 109. Hydrodyn. Lab., Dep. Civil Eng., MIT, Cambridge, Mass.
- GRASS, A. J., STUART, R. J. & MANSOUR-TEHRANI, M. 1991 Vortical structures and coherent motion in turbulent flow over smooth and rough boundaries. *Philos. Trans. R. Soc. Lond. A* **336**, 36–65.
- HALL, D. 1988 Measurements of the mean force on a particle near a boundary in turbulent flow. *J. Fluid Mech.* **187**, 451–466.
- HOFLAND, B. 2005 Rock and roll, turbulence-induced damage to granular bed protections. Ph.d, Tech. Univ. Delft.
- HOFLAND, B. & BATTJES, J. 2006 Probability density functions of instantaneous drag forces and shear stresses on a bed. *J. Hydraul. Eng.* **132** (11), 1169–1175.
- HOFLAND, B., BATTJES, J. & BOOIJ, R. 2005 Measurement of fluctuating pressures on coarse bed material. *J. Hydraul. Eng.* **131** (9), 770–781.
- JACKSON, P. S. 1981 On the displacement height in the logarithmic velocity profile. *J. Fluid Mech.* **111**, 15–25.
- JIMÉNEZ, J. 2004 Turbulent flow over rough walls. *Annu. Rev. Fluid Mech.* **36**, 173–196.
- JIMÉNEZ, J. & HOYAS, S. 2008 Turbulent fluctuations above the buffer layer of wall-bounded flows. *J. Fluid Mech.* **611**, 215–236.
- KIM, I., ELGHOBASHI, S. & SIRIGNANO, W. A. 1993 Three-dimensional flow over two spheres placed side by side. *J. Fluid Mech.* **246**, 465–488.
- KIM, J. 1989 On the structure of pressure fluctuations in simulated turbulent channel flow. *J. Fluid Mech.* **205**, 421–451.
- KIM, J., MOIN, P. & MOSER, R. 1987 Turbulence statistics in fully developed channel flow at low Reynolds number. *J. Fluid Mech.* **177**, 133–166.
- KING, M. R. & LEIGHTON, D. T. J. 1997 Measurement of the inertial lift on a moving sphere in contact with a plane wall in a shear flow. *Phys. Fluids* **9** (5), 1248–1255.
- KRISHNAN, G. P. & LEIGHTON, D. T. J. 1995 Inertial lift on a moving sphere in contact with a plane wall in a shear flow. *Phys. Fluids* **7** (11), 2538–2545.

- LEE, H. & BALACHANDAR, S. 2010 Drag and lift forces on a spherical particle moving on a wall in a shear flow at finite Re. *J. Fluid Mech.* **657**, 89–125.
- LEE, J. H., SUNG, H. J. & KROGSTAD, P.-A. 2011 Direct numerical simulation of the turbulent boundary layer over a cube-roughened wall. *J. Fluid Mech.* **669**, 397–431.
- LEE, S.-H. & SUNG, H. J. 2007 Direct numerical simulation of the turbulent boundary layer over a rod-roughened wall. *J. Fluid Mech.* **584**, 125–146.
- LEONARDI, S., ORLANDI, P. & ANTONIA, R. A. 2007 Properties of d- and k-type roughness in a turbulent channel flow. *Phys. Fluids* **19** (12), 125101.
- LEONARDI, S., ORLANDI, P., SMALLEY, R. J., DJENIDI, L. & ANTONIA, R. A. 2003 Direct numerical simulations of turbulent channel flow with transverse square bars on one wall. *J. Fluid Mech.* **491**, 229–238.
- LIGRANI, P. M. & MOFFAT, R. J. 1986 Structure of transitionally rough and fully rough turbulent boundary layers. *J. Fluid Mech.* **162**, 69–98.
- LUCCI, F., FERRANTE, A. & ELGHOBASHI, S. 2010 Modulation of isotropic turbulence by particles of Taylor length-scale size. *J. Fluid Mech.* **650**, 5–55.
- MANES, C., POKRAJAC, D. & MCEWAN, I. 2007 Double-averaged open-channel flows with small relative submergence. *J. Hydraul. Eng.* **133** (8), 896–904.
- MANES, C., POKRAJAC, D., NIKORA, V. I., RIDOLFI, L. & POGGI, D. 2011 Turbulent friction in flows over permeable walls. *Geophys. Res. Lett.* **38** (3), L03402–.
- MARUSIC, I., MCKEON, B. J., MONKEWITZ, P. A., NAGIB, H. M., SMITS, A. J. & SREENIVASAN, K. R. 2010 Wall-bounded turbulent flows at high Reynolds numbers: Recent advances and key issues. *Phys. Fluids* **22** (6), 065103.
- MOLLINGER, A. & NIEUWSTADT, F. 1996 Measurement of the lift force on a particle fixed to the wall in the viscous sublayer of a fully developed turbulent boundary layer. *J. Fluid Mech.* **316**, 285–306.
- MUTHANNA, C., NIEUWSTADT, F. T. M. & HUNT, J. C. R. 2005 Measurement of the aerodynamic forces on a small particle attached to a wall. *Exp. Fluids* **39**, 455–463.
- NAKAGAWA, H. & NEZU, I. 1977 Prediction of the contributions to the Reynolds stress from bursting events in open-channel flows. *J. Fluid Mech.* **80** (01), 99–128.
- NEZU, I. & NAKAGAWA, H. 1993 *Turbulence in Open-Channel Flows*. IAHR/AIRH Monograph Series, Balkema Publishers.
- NIKORA, V., MCEWAN, I., MCLEAN, S., COLEMAN, S., POKRAJAC, D. & WALTERS, R. 2007 Double-averaging concept for rough-bed open-channel and overland flows: Theoretical background. *J. Hydraul. Eng.* **133** (8), 873–883.
- NIKORA, V. I., GORING, D. G., MACEWAN, I. & GRIFFITHS, G. 2001 Spatially averaged open-channel flow over rough bed. *J. Hydraul. Eng.* **127** (2), 123–133.
- NIKURADSE, J. 1933 Strömungsgesetze in rauhen Röhren. *VDI-Forschungsheft* **361**, engl. translation 1950, Laws of flow in rough pipes. NACA TM 1292.
- ORLANDI, P. & LEONARDI, S. 2008 Direct numerical simulation of three-dimensional turbulent rough channels: parameterization and flow physics. *J. Fluid Mech.* **606**, 399–415.
- ORLANDI, P., LEONARDI, S., TUZI, R. & ANTONIA, R. A. 2003 Direct numerical simulation of turbulent channel flow with wall velocity disturbances. *Phys. Fluids* **15** (12), 3587–3601.



- PAPANICOLAOU, A., DIPLAS, P., EVAGGELOPOULOS, N. & FOTOPOULOS, S. 2002 Stochastic incipient motion criterion for spheres under various packing conditions. *J. Hydraul. Eng.* **128** (4), 369–380.
- PESKIN, C. S. 1972 Flow patterns around heart valves: A digital computer method for solving the equation of motion. PhD thesis, Albert Einstein College of Medicine.
- PESKIN, C. S. 2002 The immersed boundary method. *Acta Numerica* **11**, 479–517.
- PIMENTA, M. M., MOFFAT, R. J. & KAYS, W. M. 1975 The turbulent boundary layer: an experimental study of the transport of momentum and heat with the effect of roughness. Internal report HMT-21. Dep. Mech. Eng. Stanford Univ., Stanford, California 94305.
- POGGY, D., PORPORATO, A. & RIDOLFI, L. 2003 Analysis of the small-scale structure of turbulence on smooth and rough walls. *Phys. Fluids* **15** (1), 35–46.
- POKRAJAC, D., FINNIGAN, J., MANES, C., MCEWAN, I. & NIKORA, V. 2006 On the definition of shear velocity in rough bed open-channel flows. In *River Flow 2006* (ed. R. Ferreirara, E. Alves, J. Leal & A. Cardoso). A.A. Balkema, Rotterdam.
- POKRAJAC, D. & MANES, C. 2009 Velocity measurements of a free-surface turbulent flow penetrating a porous medium composed of uniform-size spheres. *Transport Porous Med.* **78**, 367 – 383.
- POPE, S. 2000 *Turbulent Flows*. Cambridge University Press.
- RAUPACH, M. R., ANTONIA, R. A. & RAJAGOPALAN, S. 1991 Rough-wall turbulent boundary layers. *App. Mech. Rev.* **44** (1), 1–25.
- VAN RIJN, L. C. 1993 *Principles of sediment transport in rivers, estuaries, and costal seas*. Aqua publications, Amsterdam, Netherlands.
- ROMA, A., PESKIN, C. & BERGER, M. 1999 An adaptive version of the immersed boundary method. *J. Comput. Phys.* **153** (2), 509–534.
- SAFFMAN, P. G. 1965 The lift on a small sphere in a slow shear flow. *J. Fluid Mech.* **22** (2), 385–400.
- SCHLICHTING, H. 1936 Experimentelle Untersuchungen zum Rauheitsproblem. *Ing. Arch.* **7**, 1–34.
- SCHLICHTING, H. 1965 *Grenzschicht-Theorie*, 5th edn. Karlsruhe: Verlag G. Braun.
- SHIELDS, A. 1936 Anwendung der Ähnlichkeitsmechanik und der Turbulenzforschung auf die Geschiebebewegung. *Mitteilungen der Versuchsanstalt für Wasserbau und Schiffbau (Berlin)* **26**.
- SHOCKLING, M. A., ALLEN, J. J. & SMITS, A. J. 2006 Roughness effects in turbulent pipe flow. *J. Fluid Mech.* **564**, 267–285.
- SINGH, K. M., SANDHAM, N. D. & WILLIAMS, J. J. R. 2007 Numerical simulation of flow over a rough bed. *J. Hydraul. Eng.* **133** (4), 386–398.
- THOM, A. S. 1971 Momentum absorption by vegetation. *Q.J.R. Meteorol. Soc.* **97** (414), 414–428.
- TOWNSEND, A. A. 1971 *The structure of turbulent shear flow*. Cambridge: Cambridge University Press.
- UHLMANN, M. 2003 New results on the simulation of particulate flows. *Tech. Rep.* 1038. CIEMAT, Madrid, Spain, ISSN 1135-9420.

- UHLMANN, M. 2005*a* An immersed boundary method with direct forcing for the simulation of particulate flows. *J. Comput. Phys.* **209** (2), 448–476.
- UHLMANN, M. 2005*b* An improved fluid-solid coupling method for DNS of particulate flow on a fixed mesh. In *Proc. 11th Workshop Two-Phase Flow Predictions* (ed. M. Sommerfeld). Merseburg, Germany: Universität Halle, ISBN 3-86010-767-4.
- UHLMANN, M. 2006*a* Direct numerical simulation of sediment transport in a horizontal channel. *Tech. Rep.*. CIEMAT, Madrid, Spain, ISSN 1135-9420.
- UHLMANN, M. 2006*b* Experience with DNS of particulate flow using a variant of the immersed boundary method. In *Proc. ECCOMAS CFD 2006* (ed. P. Wesseling, E. Oñate & J. Périaux). Egmond aan Zee, The Netherlands: TU Delft, ISBN 90-9020970-0.
- UHLMANN, M. 2008 Interface-resolved direct numerical simulation of vertical particulate channel flow in the turbulent regime. *Phys. Fluids* **20** (5), 053305.
- VERZICCO, R. & ORLANDI, P. 1996 A finite-difference scheme for three-dimensional incompressible flows in cylindrical coordinates. *J. Comput. Phys.* **123**, 402–414.
- WILLETTS, B. B. & MURRAY, C. G. 1981 Lift exerted on stationary spheres in turbulent flow. *J. Fluid Mech.* **105**, 487–505.
- YUN, G., KIM, D. & CHOI, H. 2006 Vortical structures behind a sphere at subcritical Reynolds numbers. *Phys. Fluids* **18** (1), 015102.
- ZENG, L., BALACHANDAR, S., FISCHER, P. & NAJJAR, F. 2008 Interactions of a stationary finite-sized particle with wall turbulence. *J. Fluid Mech.* **594**, 271–305.
- ZENG, L., NAJJAR, F., BALACHANDAR, S. & FISCHER, P. 2009 Forces on a finite-sized particle located close to a wall in a linear shear flow. *Phys. Fluids* **21** (3), 033302.